

PAPER

## A simple and effective method for smartphone-based detection of polyamines in oral cancer

To cite this article: Asmita Mojumdar *et al* 2024 *Biomed. Mater.* **19** 045044

View the [article online](#) for updates and enhancements.

### You may also like

- [Morphology and Magnetic Properties of Iron Oxide Nanostructures Synthesized with Biogenic Polyamines](#)  
Sangaraju Shanmugam, Takuya Nakanishi and Tetsuya Osaka
- [Effect of spermidine on reproductive, seed quality and bio-physiological characteristics of chickpea \(\*Cicer arietinum\* L.\) genotypes under salt stress](#)  
Mamta Sawariya, Neha Yadav, Ajay Kumar et al.
- [Aromatic and heteroaromatic azacrown compounds: advantages and disadvantages of rigid macrocyclic ligands](#)  
Anastasia D. Zubenko and Olga A. Fedorova

# Breath Biopsy Conference



Join the conference to explore the **latest challenges** and advances in **breath research**, you could even **present your latest work!**



5th & 6th November  
Online



Main talks



Early career sessions



Posters

**Register now for free!**

# Biomedical Materials



## PAPER

# A simple and effective method for smartphone-based detection of polyamines in oral cancer

Asmita Mojumdar<sup>1,2</sup>, Unnikrishnan B S<sup>2,\*</sup>  and Gopinath Packirisamy<sup>1,2,\*</sup> 

<sup>1</sup> Centre for Nanotechnology, Indian Institute of Technology Roorkee, Roorkee, Uttarakhand 247667, India

<sup>2</sup> Department of Biosciences and Bioengineering, Indian Institute of Technology Roorkee, Roorkee, Uttarakhand 247667, India

\* Authors to whom any correspondence should be addressed.

E-mail: [ukbsbio@gmail.com](mailto:ukbsbio@gmail.com), [genegopi@gmail.com](mailto:genegopi@gmail.com) and [gopi@bt.iitr.ac.in](mailto:gopi@bt.iitr.ac.in)

**Keywords:** Polyamines, TA@AuNPs, microwave-assisted, nano-sensor, colourimetric sensing, oral cancer

Supplementary material for this article is available [online](#)

RECEIVED  
17 September 2023

REVISED  
23 May 2024

ACCEPTED FOR PUBLICATION  
13 June 2024

PUBLISHED  
27 June 2024

## Abstract

Oral cancer accounts for 50%–70% of all cancer-related deaths in India and ranks sixth among the most frequent cancers globally. Roughly 90% of oral malignancies are histologically arise from squamous cells and are therefore called oral squamous cell carcinoma. Organic polycations known as biogenic polyamines, for example, putrescine (Put), spermidine (Spd), and spermine (Spm), are vital for cell proliferation, including gene expression control, regulation of endonuclease-mediated fragmentation of DNA, and DNA damage inhibition. Higher Spm and Spd levels have been identified as cancer biomarkers for detecting tumour development in various cancers. The current study utilises tannic acid, a polyphenolic compound, as a reducing and capping agent to fabricate AuNPs via a one-step microwave-assisted synthesis. The fabricated TA@AuNPs were utilised as a nanoprobe for colourimetric sensing of polyamines in PBS. When TA@AuNPs are added to the polyamine, the amine groups in polyamines interact with the phenolic groups of TA@AuNPs via hydrogen bonding or electrostatic interactions. These interactions cause the aggregation of TA@AuNPs, resulting in a red shift of the Surface Plasmon Resonance band of TA@AuNPs from 530 nm to 560 nm. The nanoprobe was found to be highly specific for Spm at low concentrations. TA@AuNPs were able to detect Spm successfully in artificial saliva samples. On recording the RGB values of the sensing process using a smartphone app, it was found that as the nanoparticles aggregated due to the presence of Spm, the intensity of the *R*-value decreased, indicating the aggregation of TA@AuNPs due to interaction with the polyamine.

## 1. Introduction

Globally, oral cancer (OC) ranks sixth among the most frequent cancers [1]. It is the most prevalent disease which accounts for 50%–70% of all cancer-related deaths and has the most significant incidence in Asian nations. Oral malignancies that arise in the squamous cells of the oral cavity are called oral squamous cell carcinoma (OSCC). OSCC accounts for about 90% of the oral malignancies [2]. Any area of the oral cavity can be affected, including the anterior tongue, cheek, gingiva, and floor of the mouth [3]. Several risk factors or etiological factors of OC that have been reported to influence OC significantly are tobacco, betel quid chewing (also known as

gutka), alcohol, human papillomavirus, syphilis, orodental factors, dietary deficiencies, chronic candidiasis, viruses, old age, and genetics.

According to research on cancer tissues, there may be a connection between molecular and tissue-level changes that promote malignant changes in the tissue and is essential for the progression of the disease [4]. A biological molecule detected in tissues and other bodily fluids, that indicates an abnormal physiological condition including cancer is defined as a ‘biomarker’ by the National Cancer Institute [5]. Biomarkers are crucial in determining the occurrence of the disease. A disease’s underlying tissue alterations may exhibit changes in omics-level expressions. Nucleic acids, proteins, peptides, enzymatic

modifications, antibodies, metabolites, lipids, and carbohydrates in biofluids serve as biomarkers [6].

Blood, serum, plasma, bodily secretions (sputum, saliva), or excretions (stool, urine) are some of the bio-fluids from which biomarkers can be studied. Bio-fluid samples can be collected for biomarker research using non-invasive [7], minimally invasive, or invasive techniques [8]. The prognosis for OC patients remains severe despite advancements in treatment, with a 62% 5 year survival rate [9, 10]. Late diagnosis and ineffective treatments are primarily responsible for the short survival time. In addition to early detection, established tumour markers for OSCC may aid in therapy monitoring. Surveying the existing literature, studies on the function of salivary biomarkers in OSCC patients using saliva as a diagnostic tool [11–16] have recently increased. Saliva is a readily available bio-fluid that can be collected easily and used for diagnosis as well as for continuous treatment monitoring, provided appropriate biomarkers are available.

Genetic and epigenetic mutations have a role in the complex carcinogenesis process [17]. Earlier diagnosis can improve the livelihood of the patient [18]. For diagnosing OSCC, the conventional biopsy method is regarded as the gold standard. However, due to its invasiveness, and requirement for skilled personnel and equipment, it is inconvenient for broad population screening and monitoring of patients [19]. Therefore, looking into biological molecules that serve as biomarkers is crucial because they may offer helpful diagnostic information on OSCC [17]. Globally, a very active area of research is the investigation of biomarkers for chronic illnesses and malignant neoplasms [5]. Modern analytical methods are used in metabolomics to identify and investigate metabolic changes in people undergoing pathophysiological processes, pharmaceutical interventions, or genetic mutations [20–22].

For metabolomic research, biofluids such as urine, blood, and saliva are frequently used as clinical specimens from patients [18]. Saliva is an oral fluid that can provide insight into a person's overall and oral health [23]. Proteins, peptides, nucleic acids, enzymes, hormones, antibodies, electrolytes, antimicrobial components, growth factors, and other molecules relevant to individuals' phenotypes and diseases are present in saliva [24–26]. Saliva primarily functions in digestion, swallowing, taste, and oral mucosal lubrication. However, it is well known that due to its complex and valuable composition, saliva also serves as a protective substance against toxins and pathogens in addition to the functions mentioned above [27].

Prior research studies have discovered metabolomic indicators for OSCC [28–34]. Some of them investigated salivary metabolites [35–43]. The oral microbiota [29, 44], food consumption [37–39, 45],

overall oral health state [46], and even sample collection time [39, 47] can all affect the metabolites profile, making it difficult to standardise salivary assays without sacrificing consistency and repeatability. Nevertheless, prior research has demonstrated consistent differences between OSCC and healthy patients [37], primarily due to saliva contacting the OC lesion directly [38].

All eukaryotes contain the organic polycations known as biogenic polyamines (PAs); for example, putrescine [ $\text{NH}_2(\text{CH}_2)_4\text{NH}_2$ ] (Put), spermidine [ $\text{NH}_2(\text{CH}_2)_4\text{NH}(\text{CH}_2)_3\text{NH}_2$ ] (Spd), and spermine [ $\text{NH}_2(\text{CH}_2)_3\text{NH}(\text{CH}_2)_4\text{NH}(\text{CH}_2)_3\text{NH}_2$ ] (Spm). These PAs are vital for cell proliferation [48–50], including gene expression control, regulation of endonuclease-mediated fragmentation of DNA, and DNA damage inhibition, respectively. These polyamines, being positively charged due to the protonation of their primary and secondary amino groups at physiological pH, interact electrostatically with negatively charged molecules like DNA, RNA, proteins, and phospholipids [51]. It has been suggested that these polyamines control cellular activities at the transcriptional, translational, and post-translational levels. In contrast to inorganic cations like  $\text{Ca}^{2+}$  or  $\text{Mg}^{2+}$ , polyamines can engage in hydrophobic interactions via their flexible methylene chains as their positive charges are placed at defined distances [52].

Generally, complex multiple feedback processes at the level of catabolism, biosynthesis, absorption, and efflux are used to maintain polyamine homeostasis intricately [49, 50, 53, 54]. It is significant to note that many pathways control spermine and spermidine levels and that changes in these levels may signal altered biological processes related to cancer [54]. As a result, higher spermine and spermidine levels have been identified as cancer biomarkers for detecting tumour development in various cancers. A study by Song *et al*, 2020 [38] showed that biogenic polyamines were upregulated in the saliva of OSCC patients compared to patients with premalignant lesions and healthy patients. Another study by de Sá Alves *et al*, 2021 [55] showed that polyamines could be potentially promising salivary biomarkers for the early detection of OSCC. Therefore, developing novel diagnostic tools for identifying spermidine and spermine in biological samples with small sample volumes is vital.

Although several analytical techniques such as gas chromatography, capillary electrophoresis, HPLC, mass spectrophotometry etc were used to determine spermine and spermidine in biological samples [56] they are time-consuming, and some strategies are expensive. Additionally, because spermidine and spermine are aliphatic substances, they do not naturally absorb UV light or show any fluorescence resulting in more difficulty in their detection [57].

Certain optical based assays were also developed for detection of spermine and spermidine using organic polymers [58], small molecule chromophores [59], amphiphile-based chemo-sensor [60], coordination compounds [61], di-carboxylated ethynyl arene as a fluorescent chemo sensor in the presence of metal ions [62]. These techniques are either non-detectable or have more significant detection limits for spermidine and spermine. Therefore, effective clean-up and pre-concentration procedures are necessary for the high selectivity and sensitivity of the detection of both analytes [57]. Many literature states the detection of spermine and spermidine using various methods like colourimetric detection using phenolphthalein derivatives having two crown ethers [63], Pt- or Pd-complexes for chelation of spermine [64], prussian blue screen-printed electrode as a biosensor [65], quinoline-modified- $\beta$ -cyclodextrin used for synthesising molecularly imprinted fluorescent chemo-sensor [66],  $\text{Fe}^{3+}$  displacement assay by fluorescent organic nanoparticles for selective chemo-sensing [67], colourimetric and fluorometric detection using Tyr-AuNPs [57], visual detection using organic nanoparticles [68], zincon based colourimetric detection [69], carbon nanotube based electrolyte gated field-effect transistor [70], and blue carbon dots and yellow quantum dots as a ratiometric fluorescent nanoprobe for detection [71].

The well-defined nanostructures of AuNPs have attracted much attention in recent years. AuNPs can integrate excellent surface/interface recognition ability and have distinctive optical properties. AuNPs have become popular as prompt visual reporters by rationally designing the AuNPs utilising their surface chemistry [72–74]. Reducing chloroauric acid with various organic compounds generally acts as the simplest method of producing AuNPs [75]. To change the uses of AuNPs, the functionalisation of the surface of AuNPs should be carried out to improve a variety of factors, such as biocompatibility, minimise toxicity, and synthesis of AuNPs with different molecular probes for analysing diverse bio-species. Previous work has been done in our lab using graphene oxide nanosheets that were modified with gold nanoparticles for detection of carcinoembryonic antigen for cancer detection [76].

Tannic acid, a polyphenolic compound, comprises a core glucose molecule with one or more galloyl residues attached to its hydroxyl groups. Tannic acid has multiple functions: an antioxidant agent [77], utilised as a food additive [78] and is said to have anti-carcinogenic and anti-mutagenic properties [77]. Tannic acid has been reported to prevent fore stomach, lung, and skin tumours in mice induced by N-methyl-N-nitrosourea and polycyclic aromatic hydrocarbon carcinogens [77, 79, 80]. Tannic acid-capped gold nanoparticles (TA@AuNPs) have been used for various heavy metal detection,

such as  $\text{Pb}^{2+}$  by using TA@AuNPs as nanozymes [81],  $\text{Zn}^{2+}$  and  $\text{Hg}^{2+}$  employing TA@AuNPs and utilising their redox activities [82]. However, as per our understanding, first time we have reported the microwave mediated synthesis of TA@AuNPs for polyamine sensing in OC.

## 2. Materials

To synthesise TA@AuNPs, tannic acid and gold chloride hydrate (tetra chloroauric acid) were bought from Sisco Research Laboratories Private Limited, India (SRL Chemical). For TA@AuNPs stability studies, buffer solutions of pH 4, 7 and 9.2, sodium chloride, calcium chloride dihydrate and lysozyme were bought from SRL Chemical, India. PBS powder, potassium phosphate dibasic anhydrous, magnesium nitrate hexahydrate and sodium bicarbonate were purchased from HiMedia for stability studies. All other chemicals of analytical grade were purchased from SRL, India. Artificial saliva (CAS No.- 7732-18-5) was purchased from BIOCHEMAZONE®, Canada.

## 3. Methods

### 3.1. Synthesis and characterisation of TA@AuNPs

TA@AuNPs were fabricated via the microwave-assisted synthesis method by reduction of  $\text{Au}^{3+}$  to  $\text{Au}^0$  by tannic acid, which also acted as the capping agent using microwave energy for the reduction process. For the synthesis procedure, a microwave Panasonic NN-ST26JM model was used with a power of 800 watts. Firstly, 0.1 mM  $\text{HAuCl}_4$  was kept in a microwave for 7 s. Immediately, various concentrations of tannic acid solution (0.05, 0.1, 0.15, 0.2, 0.25% w/v) was added to the salt solution and kept in the microwave for another 3–5 s. The colour formation and stability were observed for time period of 24 h. The appearance of a red colour indicated the formation of TA@AuNPs. All the stock concentrations and working concentrations for the preparation of TA@AuNPs was prepared in Milli-Q water (Merck Millipore). The prepared TA@AuNPs were stored at 4 °C for further characterisation and studies.

UV-Visible spectroscopic analysis of TA@AuNPs was performed using a microplate spectrophotometer (BioTek Epoch, Agilent, USA). The hydrodynamic size of TA@AuNPs was determined using the Malvern Zetasizer Nano series (Nano-ZS90) instrument. Thin film x-ray diffraction of TA@AuNPs was performed using Rigaku Smart Lab x-ray diffractometer using a  $\text{Cu-K}\alpha$  source (1.54 Å) to index the planes present in TA@AuNPs. Samples for XRD was prepared by adding 10  $\mu\text{l}$  of TA@AuNPs on a small glass piece and then dried (layer-by-layer). The process was repeated till a thin of TA@AuNPs formed on the glass piece. XRD was performed from a starting  $2\theta$  angle of 2° to



2 $\theta$  ending angle of 90° with a step size of 0.02°. TEM analysis was performed using FEI Tecnai G2 20S-Twin High-Resolution Transmission Electron Microscope having LaB<sub>6</sub> or W as the electron source to determine the nanoparticle shape and size. Samples for TEM analysis were prepared by dropping 20  $\mu$ l of TA@AuNPs on a copper 200 mesh grid and then dried. FTIR analysis was performed using Agilent Cary 630 FTIR instrument to determine the functional groups in TA responsible for stabilising and reducing gold nanoparticles. TA@AuNPs were lyophilised, and the lyophilised samples were used for FTIR analysis.

### 3.2. Stability studies of TA@AuNPs

TA@AuNPs (400  $\mu$ l) were incubated at different temperatures (4 °C, 25 °C, 37 °C and 60 °C) to assess the impact of temperature on the nanoparticles. After an incubation period of 24 h, the spectral scan of the nanoparticles was done on the BioTek Epoch microplate reader from 400 nm to 700 nm. TA@AuNPs were incubated with PBS (pH 7.4) (ratio of 1:1 for PBS:TA@AuNPs) in a micro-well plate and read using the microplate reader from 400 nm to 700 nm. The incubated nanoparticles were monitored for 0, 1, 2, 3, 4 and 5 h to examine any Surface Plasmon Resonance (SPR) shift of TA@AuNPs due to aggregation caused by PBS. TA@AuNPs were incubated with buffers of pH 4, pH 7 and pH 9.2 (ratio of 1:1 for each buffer:TA@AuNPs) in a micro-well plate and spectral scan from 400 nm to 700 nm was performed at 0, 1, 2, 3, 4 and 5 h in the microplate reader. Stocks of various salts (NaCl, CaCl<sub>2</sub>·2H<sub>2</sub>O, K<sub>2</sub>HPO<sub>4</sub>, Mg(NO<sub>3</sub>)<sub>2</sub>·6H<sub>2</sub>O and NaHCO<sub>3</sub>) were prepared and then each salt was diluted to various concentrations of 0.16  $\mu$ M, 0.31  $\mu$ M, 0.62  $\mu$ M, and 1.25  $\mu$ M. The dilutions of each salt were added to a 96-well plate and then incubated with TA@AuNPs (ratio of 1:1 for each salt concentrations: TA@AuNPs) for 5 h. A spectral scan was taken at each hour to monitor the impact of the salts on TA@AuNPs using a microplate reader. The stock solution of lysozyme was prepared in PBS at a concentration of 10 mg ml<sup>-1</sup>. Lysozyme (2.2  $\mu$ g ml<sup>-1</sup>) was added to a micro-well plate and then incubated with TA@AuNPs (ratio of 1:1 for lysozyme: TA@AuNPs) over 5 h. A spectral scan was taken at each hour to monitor the influence of lysozyme on TA@AuNPs using a microplate reader.

### 3.3. Identification and specificity study of polyamine sensing

Putrescine, spermidine and spermine stocks were prepared in MilliQ water (Millipore). Each polyamine was diluted to various concentrations of 0.01  $\mu$ M, 0.02  $\mu$ M, 0.04  $\mu$ M, 0.08  $\mu$ M, 0.15  $\mu$ M, 0.30  $\mu$ M, 0.61  $\mu$ M, 1.22  $\mu$ M, 2.24  $\mu$ M, 5  $\mu$ M, 10  $\mu$ M, 20  $\mu$ M, 40  $\mu$ M, 78  $\mu$ M, and 156  $\mu$ M. Each dilution of each polyamine was added to a micro-well plate followed

by the addition of TA@AuNPs in a ratio of 1:1 of each polyamine concentration: TA@AuNPs and incubated for 15 min at room temperature. After the incubation, a spectral scan was performed from 400 nm to 700 nm in the microplate reader. In order to determine the limit of detection (LOD) for Spm and Spd sensing by TA@AuNPs, each dilution of Spd and Spm was added to TA@AuNPs (in a ratio of 1:3 for each dilution of Spd and Spm: TA@AuNPs), incubated for 15 min and the absorbance data at 560 nm was recorded in triplicates for each set using a UV-Visible spectrophotometer. The LOD of polyamines sensed using TA@AuNPs was determined using the following mathematical equation from the calibration curve:

$$\text{LOD} = 3.3 \left( \frac{\sigma}{m} \right)$$

where,  $\sigma$  = standard deviation of the response and  $m$  = slope of the calibration curve [83].

Stocks of different amino acids like L-Leucine, dopamine, L-Lysine, L-Histidine, L-Cysteine, L-Arginine, and L-Serine were made. Based on the sensitivity study, we have selected 1.22  $\mu$ M concentration of each amino acids and polyamines and added in a micro-well plate and then incubated for 15 min with TA@AuNPs (in a ratio of 1:1 for each amino acid: TA@AuNPs). After the incubation period of 15 min, the absorbance of all the amino acid and polyamine were read using the micro-plate reader at a particular wavelength. All the experiments were performed in triplicates.

### 3.4. Colourimetric sensing of polyamines using nanodrop spectrophotometry

Different concentrations of Spd (10, 20, 39, 312, 625, and 1250  $\mu$ M) and Spm (39, 52, 156, 312, 625, 1250, and 2500  $\mu$ M) were incubated with TA@AuNPs (in a ratio of 1:2 for each polyamine concentration: TA@AuNPs) for 15 min. 5  $\mu$ l of the nanoparticle incubated Spd and Spm dilutions were then used to measure absorbance at 560 nm using the DeNovix DS-11+ Spectrophotometer. The control TA@AuNPs were used as blank for background subtraction. All the experiments were performed in triplicates.

### 3.5. Smartphone-based detection of polyamine

Different concentrations (0.08, 0.15, 0.30, 0.61, 1.22, 2.5, 5, 10, 20, 39, 78, 156, 312.5, 625, 1250, 2500 and 5000  $\mu$ M) of each Spd and Spm were incubated with TA@AuNPs (in a ratio of 1:2 for each concentration of polyamine: TA@AuNPs) for 15 min. The samples were kept in a glass cuvette and placed at a particular distance. The images of samples were acquired using a smartphone equipped with a camera and an App (Colorimeter) that computes and display RGB intensities. The percentage of RGB values of each concentration of Spd as well as Spm was measured and compared with control TA@AuNPs.

### 3.6. Colourimetric sensing of polyamines in artificial saliva

Different concentrations of Spm (0.01  $\mu\text{M}$ , 0.02  $\mu\text{M}$ , 0.04  $\mu\text{M}$ , 0.08  $\mu\text{M}$ , 0.15  $\mu\text{M}$ , 0.30  $\mu\text{M}$ , 0.61  $\mu\text{M}$ , 1.22  $\mu\text{M}$ , 2.24  $\mu\text{M}$ , 5  $\mu\text{M}$ , 10  $\mu\text{M}$ , 20  $\mu\text{M}$ , 40  $\mu\text{M}$ , 78  $\mu\text{M}$ , and 156  $\mu\text{M}$ ) were prepared and each concentration was spiked in artificial saliva. The spiked samples were added to a micro-well plate and incubated with TA@AuNPs (in a ratio of 1:1 for each concentration of polyamine: TA@AuNPs) for 15 min. A spectral scan from 400 to 700 nm of all the concentrations was performed after 15 min. Similarly, each dilution of Spm (0.01  $\mu\text{M}$ , 0.02  $\mu\text{M}$ , 0.04  $\mu\text{M}$ , 0.08  $\mu\text{M}$ , 0.15  $\mu\text{M}$ , 0.30  $\mu\text{M}$ , 0.61  $\mu\text{M}$ , 1.22  $\mu\text{M}$ , 2.24  $\mu\text{M}$ , 5  $\mu\text{M}$ , 10  $\mu\text{M}$ , 20  $\mu\text{M}$ , 40  $\mu\text{M}$ , 78  $\mu\text{M}$ , and 156  $\mu\text{M}$ ) was spiked in artificial saliva and TA@AuNPs (in a ratio of 1:1:2 of each dilution of Spm: artificial saliva: TA@AuNPs) was added to each spiked sample and incubated for 15 min. Absorbance data at a fixed wavelength (560 nm) was collected for all the spiked samples in triplicates using a UV-Visible spectrophotometer for determination of the calibration curve for LOD determination. LOD was determined using the same formula mentioned previously from the calibration curve. Different concentrations of Spm (final concentrations of 0.05, 0.1, 0.2, 0.41, 0.81, 1.66, 3.33, 6.66, 13.33, 26, 52, 104.16, 208.33, 416.66, 833.33, 1666.66, and 3333.33  $\mu\text{M}$ ) was spiked in artificial saliva and then incubated with TA@AuNPs (in a ratio of 1:1:2 for each concentration of Spm: artificial saliva: TA@AuNPs) for 15 min. 5  $\mu\text{l}$  of each spiked sample (13, 26, 52, 104, 208, 417, and 1667  $\mu\text{M}$ ) was used to record absorbance value at 560 nm using nanodrop spectrophotometer and the remaining sample was kept in a glass cuvette and then placed at a particular distance for smartphone-based detection. The colourimetric smartphone app was used to record the RGB intensities for each spiked sample and then compared with the control TA@AuNPs.

### 3.7. Statistical analysis

All experiments were done in triplicates. The results are expressed as mean  $\pm$  S.D. The graphs were constructed using Origin software (OriginLab Corporation, US). Statistically significant differences at  $*P < 0.01$ ,  $**P < 0.001$ ,  $***P < 0.0001$  were represented using ANOVA analysis (GraphPad Prism 9.5.).

## 4. Results and discussion

### 4.1. Characterisation of TA@AuNPs

TA@AuNPs synthesized using microwave synthesis method is depicted in figure 1(a). The prepared TA@AuNPs with varying concentrations of tannic acid during synthesis and after 24 h of stability test is shown in figures S1 and S2. The appearance of

red colour of the nanoparticles indicates the formation of gold nanoparticles. TA@AuNPs prepared using 0.05% w/v final concentration of TA (Set 2, figures S1 and S2) was used for further study based on its stability after 24 h of incubation. UV-Visible spectroscopy of the nanoparticles revealed the SPR peak of TA@AuNPs at 530 nm (figure 1(b)). XRD of a thin film of TA@AuNPs was also performed which is depicted in figure 1(c). Four prominent diffraction peaks are observed in the XRD pattern indexed to be (111), (200), (220) and (311) reflections of face-centered cubic (fcc) of gold metal nanoparticles, respectively. This indicates that the synthesised TA@AuNPs comprise pure crystalline gold (JCPDSno. 04-0784). The intensity of the peak that corresponds to the (111) plane is higher than the other three peaks indicating that the (111) plane is the predominant orientation for the growth of the nanoparticles [84].

TEM images of TA@AuNPs showed that the shape of the synthesised nanoparticles is almost spherical (figure 2(a)) and the selected area electron diffraction pattern of TA@AuNPs indicates that the nanoparticles are crystalline in nature (figure 2(b)). The diffraction rings from the inner to the outer was indexed to be (111), (200), (220) and (311) which correspond to the reflections of fcc gold. The fringe spacing calculated from the pattern is 0.23 nm which is comparable to the d-spacing between the fcc gold (111) plane. The particle size distribution of TA@AuNPs were also determined as depicted in figure 2(c). The fabricated TA@AuNPs were found to have an average size of  $10 \pm 4$  nm as shown in the histogram plot taking a sample set of  $n = 71$ .

The hydrodynamic size of TA@AuNPs was determined. From figure S3, we can see three peaks. Peak 1, with an intensity of 90.5%, showed a size of  $34.50 \text{ nm} \pm 16.86$ ; peak 2, with an intensity of 6.3%, showed a size of  $0.7741 \text{ nm} \pm 0.1055$ , and peak 3, with an intensity of 3.1%, showed a size of  $3932 \text{ nm} \pm 1107$ . Thus, the average hydrodynamic size is determined to be 24.70 nm with a polydispersity index value of 0.415. Similarly, the zeta potential of TA@AuNPs was also determined (figure S4). TA@AuNPs have a zeta potential of  $-24.3 \text{ mV} \pm 5.13$ . Since the pH value of AuNPs coated by TA is 2.83 which is lower than the  $\text{pK}_a$  value of TA, the gallic acid units that make TA are likely ionised partially in acidic media because of their molecular weight or steric hindrance at the hydroxyl para-carbonyl position. The phenols in tannic acid take part in redox reactions by forming quinones and donating electrons. The electrons which are donated reduce the oxidised metal ions in metal salts to form corresponding metal nanoparticles [85, 86]. Furthermore, resonance stabilises the hydroxyl meta-carbonyl position more effectively than its conjugate base. Therefore, in these situations, the dissociated functional groups

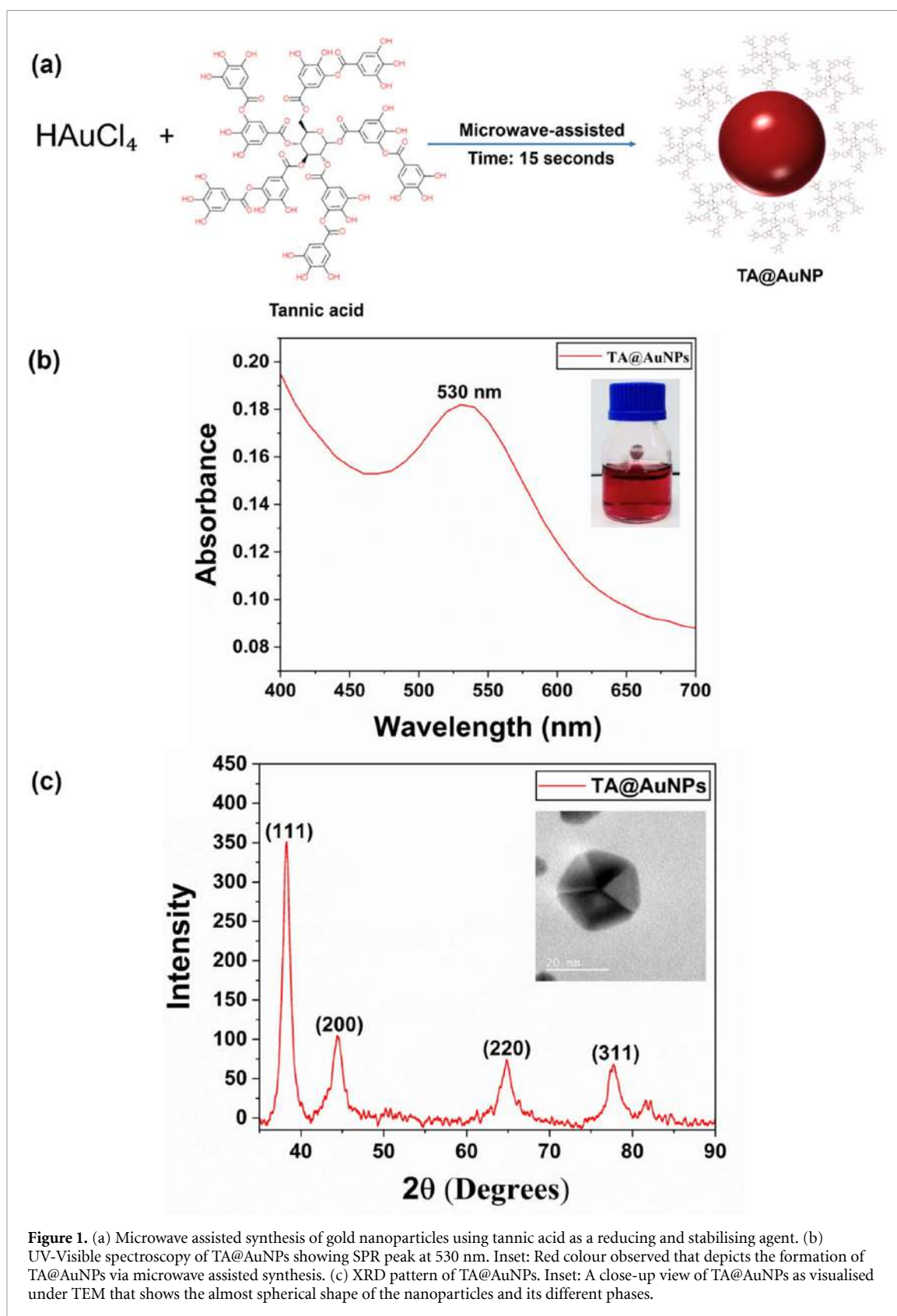


**Figure 1.** (a) Microwave assisted synthesis of gold nanoparticles using tannic acid as a reducing and stabilising agent. (b) UV-Visible spectroscopy of TA@AuNPs showing SPR peak at 530 nm. Inset: Red colour observed that depicts the formation of TA@AuNPs via microwave assisted synthesis. (c) XRD pattern of TA@AuNPs. Inset: A close-up view of TA@AuNPs as visualised under TEM that shows the almost spherical shape of the nanoparticles and its different phases.

and adsorbed polyphenolic compounds present in the structures of TA cause a charge unbalance on the surface of TA@AuNPs, which is most likely the cause of the negative values of the zeta potential displayed by the colloidal dispersions. Therefore, it can be concluded that gold nanoparticles capped by tannic acid

are stable, and TA is an efficient stabiliser for capping gold nanoparticles.

The FTIR bands for only tannic acid and TA@AuNPs have been shown in figure S5. Intense bands at 1709, 1610, 1444, 1316, 1195 and 1027  $\text{cm}^{-1}$  were observed in the FTIR spectrum of TA@AuNPs.

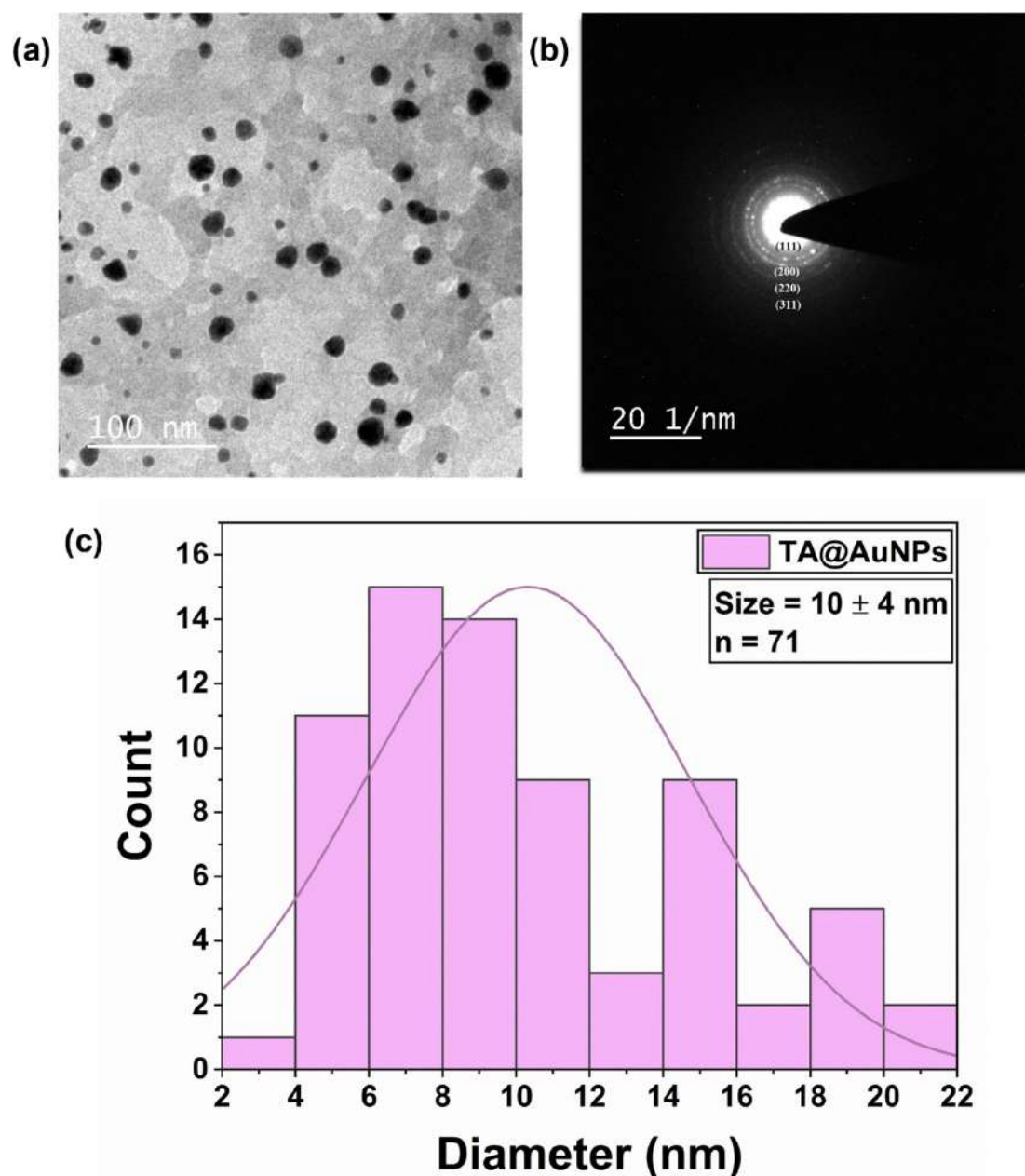


**Figure 2.** (a) TEM images of TA@AuNPs at 100 nm magnification. (b) SAED pattern of TA@AuNPs. (c) Size distribution of TA@AuNPs.

Stretching vibrations of the C=O group of carboxylic acid were indicated by an intense band around  $1709\text{ cm}^{-1}$ . The band at  $1610\text{ cm}^{-1}$  depicts stretching vibrations of C=C of the aromatic ring in tannic acid. At  $1444\text{ cm}^{-1}$ , the bend in TA's plane of C–O–H of the O–H groups was observed. The C–O stretch of tannic acid was observed at  $1316\text{ cm}^{-1}$ . The band at  $1195\text{ cm}^{-1}$  corresponds to the C–O stretching in polyols, and the band at  $1027\text{ cm}^{-1}$  is due to the bending mode of C–O–C. The binding of tannic acid to gold nanoparticles may alter the vibrational properties of the aromatic rings, resulting in changes in the observed FTIR spectra. Thus, it can be concluded that the acidic groups of tannic acid bind to the surface of

the gold nanoparticles and the phenolic groups cause the reduction of  $\text{Au}^{3+}$  to  $\text{Au}^0$ . The data supports the reducing and capping ability of tannic acid in the formation of TA@AuNPs [84, 87–90].

#### 4.2. Stability studies of TA@AuNPs

The effect of temperature on TA@AuNPs was performed to determine any aggregation of TA@AuNPs at different temperatures resulting in a shift of the SPR peak. Ideally, the sensing should be done at room temperature, i.e.  $25\text{ }^{\circ}\text{C}$ . However, since practically room temperature varies from place to place and with seasons, it was essential to determine the effect of temperature on TA@AuNPs. Figure S6 in the



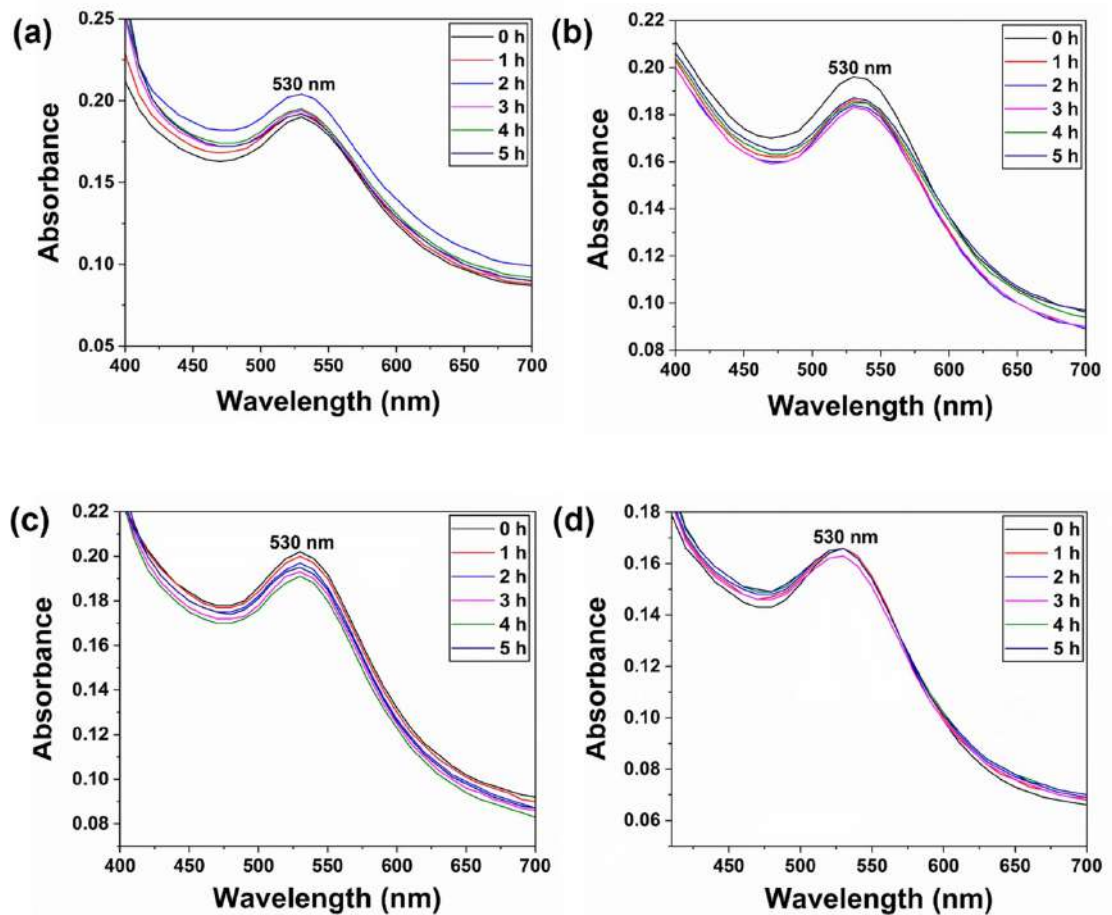


**Figure 3.** (a) Graph depicting SPR peak of TA@AuNPs incubated with PBS for 5 h. Graphs depicting SPR peak of TA@AuNPs incubated with different pH of (b) pH 4, (c) pH 7 and (d) pH 9.2 for 5 h.

supplementary shows the effect of temperature on TA@AuNPs. The graph reveals that even after 24 h of incubation at different temperatures, the SPR peak of TA@AuNPs did not shift from 530 nm. The inset show TA@AuNPs after 24 h of incubation at different temperatures. It can be observed that there was no visible colour change due to the incubation of TA@AuNPs at different temperatures, i.e. no aggregation of TA@AuNPs occurs. Thus, it can be concluded that TA@AuNPs were stable over a wide temperature range of 4 °C–60 °C.

The development of colour and the aggregation of the TA@AuNPs for the colourimetric sensing process is influenced by the sensing medium pH [84]. In the current study, PBS was used as a medium for sensing polyamines. So, it was essential to determine the effect of PBS on TA@AuNPs. Figure 3(a) shows the effect of PBS on TA@AuNPs. From the graph, it can be observed that the SPR peak of TA@AuNPs did not shift from 530 nm even after 5 h of incubation. Thus, it can be concluded that PBS did not cause any aggregation of TA@AuNPs as the SPR peak was not shifted. TA@AuNPs seem to be stable in PBS till 5 h.

The pH of saliva typically ranges from 6.2 to 7.6, with average value of 6.7. The mouth's resting pH does not drop below 6.3. Saliva helps keep the oral cavity's pH close to neutral (6.7–7.3) [91]. Salivary pH of less than 7.0 typically signifies acidemia (increased production of acid in the body). Tumours cause anaerobic metabolism of glucose, resulting in hypoxia. As a result, the pH of the surrounding environment becomes acidic in tumour conditions. The acidic environment makes it easier for the tumour cells to thrive and proliferate [92]. Thus, it is essential to determine the effect of change in pH on TA@AuNPs to find any significant shift in the SPR peak. Figures 3(b)–(d) shows the effect of (b) pH 4, (c) pH 7 and (d) pH 9.2 on TA@AuNPs. It can be observed from the graphs that the SPR peak of TA@AuNPs did not shift from 530 nm even after 5 h of incubation in buffers having different pH, indicating that no aggregation had occurred due to a change in pH. Thus, these graphs revealed that TA@AuNPs were stable over a pH range of 4–9.2 highlighting its advantage in cancer diagnostics.

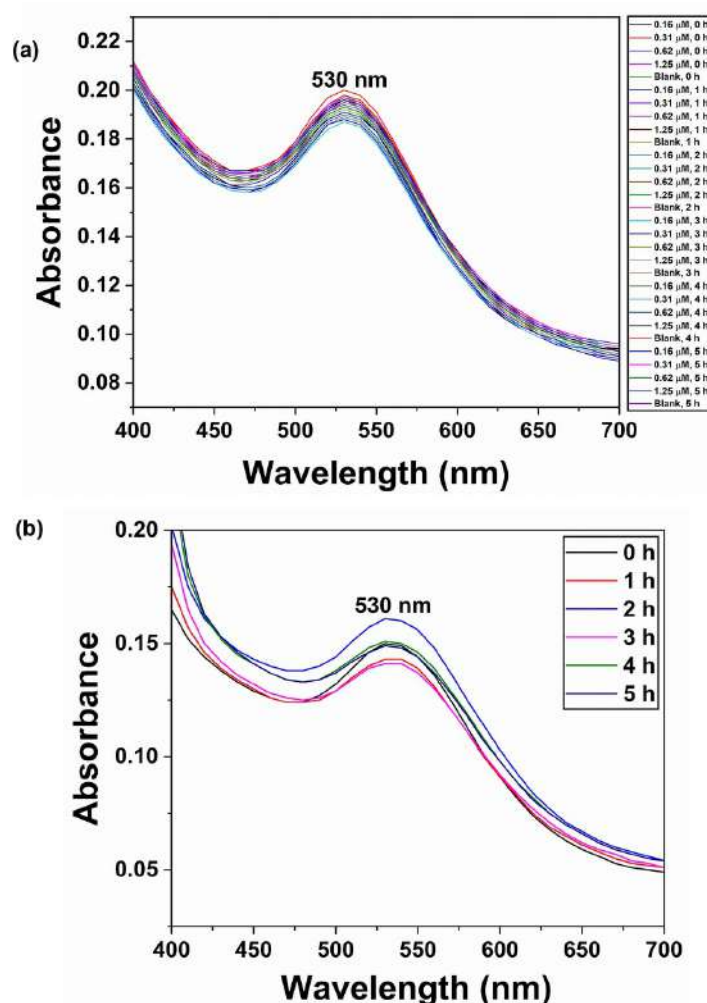


**Figure 4.** (a) Graph depicting SPR peak of TA@AuNPs incubated with different NaCl concentrations over 0–5 h. (b) Graph depicting SPR peak of TA@AuNPs incubated with lysozyme over a period of 0–5 h.

Saliva comprises 99% water and only 1% of proteins and salts. The optimum pH range of 6.0–7.5 of saliva is maintained by three buffer systems: bicarbonate, phosphate, and protein. Oversaturation of saliva with calcium hydroxyapatite under normal physiological conditions prevents demineralisation of the teeth [93]. Thus, it was crucial to determine the impact of salts present in the saliva on TA@AuNPs. Figure 4(a) shows the effect of NaCl on TA@AuNPs while figure S7–S10 in the supplementary shows effect of other salts like (S7)  $\text{CaCl}_2 \cdot 2\text{H}_2\text{O}$ , (S8)  $\text{K}_2\text{HPO}_4$ , (S9)  $\text{Mg}(\text{NO}_3)_2 \cdot 6\text{H}_2\text{O}$ , and (S10)  $\text{NaHCO}_3$  on TA@AuNPs at different concentrations and at different time periods of 0–5 h. These graphs show that the SPR peak of TA@AuNPs exhibited negligible shift from 530 nm even after 5 h of incubation with different salt concentrations, indicating that these salts did not cause the aggregation of the gold nanoparticles. Thus, it can be concluded that TA@AuNPs remain stable even in the presence of various salts and can be effectively used in salivary diagnostics.

Lysozyme is a protein in the saliva with antimicrobial properties [93]. With the turbidimetric assay, the mean lysozyme concentration in centrifuged saliva was  $2.2 \mu\text{g ml}^{-1}$ , and with the lysoplate assay, it was  $5.9 \mu\text{g ml}^{-1}$  [94]. Thus, it was essential to determine the influence of lysozyme on the sensing process of TA@AuNPs. Figure 4(b) shows the effect of lysozyme on TA@AuNPs over a period of 0–5 h. The graph shows no change in the SPR peak of TA@AuNPs from 530 nm on incubation of the nanoparticles with lysozyme even after 5 h. This data revealed that lysozyme did not play a key role in the interaction with TA@AuNPs. Thus, it can be concluded that presence of lysozyme in the saliva had no effect on SPR peak of TA@AuNPs.

#### 4.3. Colourimetric sensing of polyamines using UV-Visible spectrophotometry

Polyamines are non-conjugated systems. As a result, they are not detected using UV-Vis Spectroscopy. As a result, TA@AuNPs were used as a colourimetric detection probe for sensing three polyamines (Put,

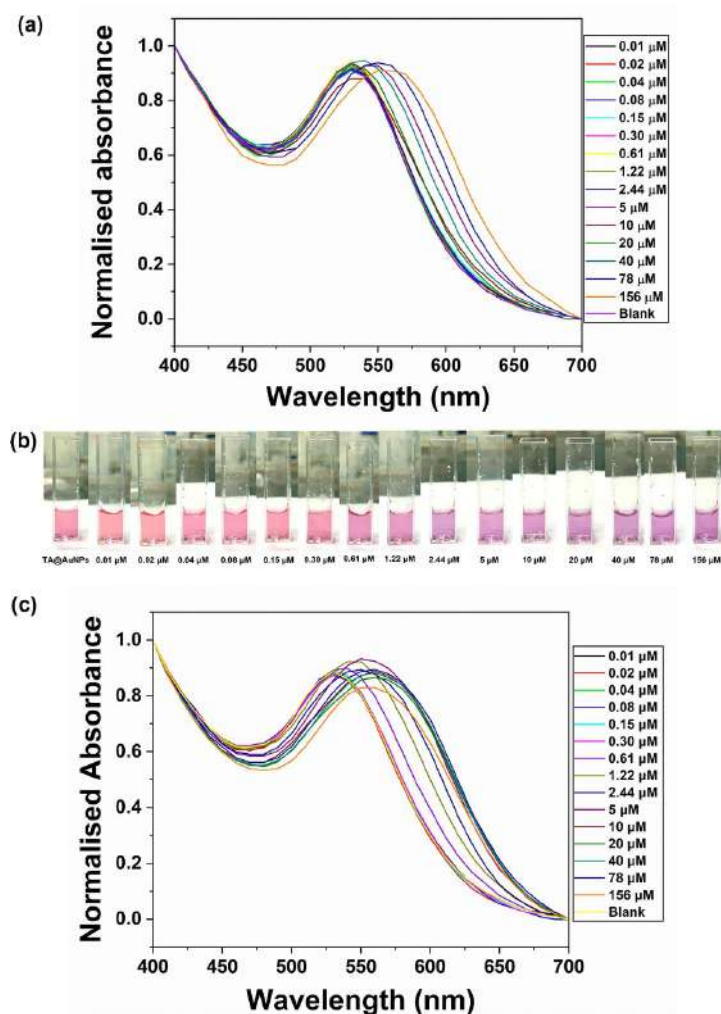


**Figure 5.** (a) Graph depicting the shift in SPR peak of TA@AuNPs when incubated with different concentrations of Spd. (b) Change in colour of TA@AuNPs from red to purple when incubated with different concentrations of Spm. (c) Graph depicting the shift in SPR peak of TA@AuNPs when incubated with different concentrations of Spm.

Spd, Spm). TA@AuNPs were incubated with different concentrations of Put, Spd and Spm and observed for any visual change in colour. The colour change was also monitored by determining the shift in SPR peak, if any, using UV-Visible Spectroscopy. Figure S11 in the supplementary shows the sensing of Put using TA@AuNPs as the colourimetric nanoprobe. The graph reveals that even with increasing concentration of Put, there was no shift in the SPR peak of TA@AuNPs. This further implies that Put had negligible interaction with TA@AuNPs that can result in their aggregation. This may be because Put has only two amine groups that do not yield sufficient interaction with TA@AuNPs, which might result in a colour change and hence a shift in the SPR peak. Thus, it can be concluded that TA@AuNPs were not specific for Put detection.

Similarly, TA@AuNPs were also incubated with Spd and Spm and observed for any visual change in colour and a consequent shift in SPR peak using UV-Visible spectroscopy. Figure 5(a) depicts the graph

that shows any shift in SPR peak on incubating different concentrations of Spd with TA@AuNPs. When Spd is incubated with TA@AuNPs, a shift is observed in the SPR peak of the nanoparticles. This indicates that Spd can aggregate TA@AuNPs resulting in the red shift of the SPR peak. This aggregation of TA@AuNPs due to Spd can be attributed to the electrostatic or hydrogen-bonded interaction of the three amine groups in Spd with the phenolic groups of TA [71]. The absorbance data for the calibration curve was recorded at 560 nm because from the spectral scan (figure 5(a)) it was observed that on aggregation of TA@AuNPs there was not only a shift in the SPR peak from 530 nm gradually to a maximum of 560 nm but there was also an increase in the intensity of the peak at 560 nm compared to the intensity at 530 nm. This increase in peak intensity at 560 nm compared to the intensity at 530 nm also signified that TA@AuNPs were aggregating resulting in a redshift in their SPR peak. Thus, the calibration curve was plotted with intensity variation at 560 nm (figure S12) for

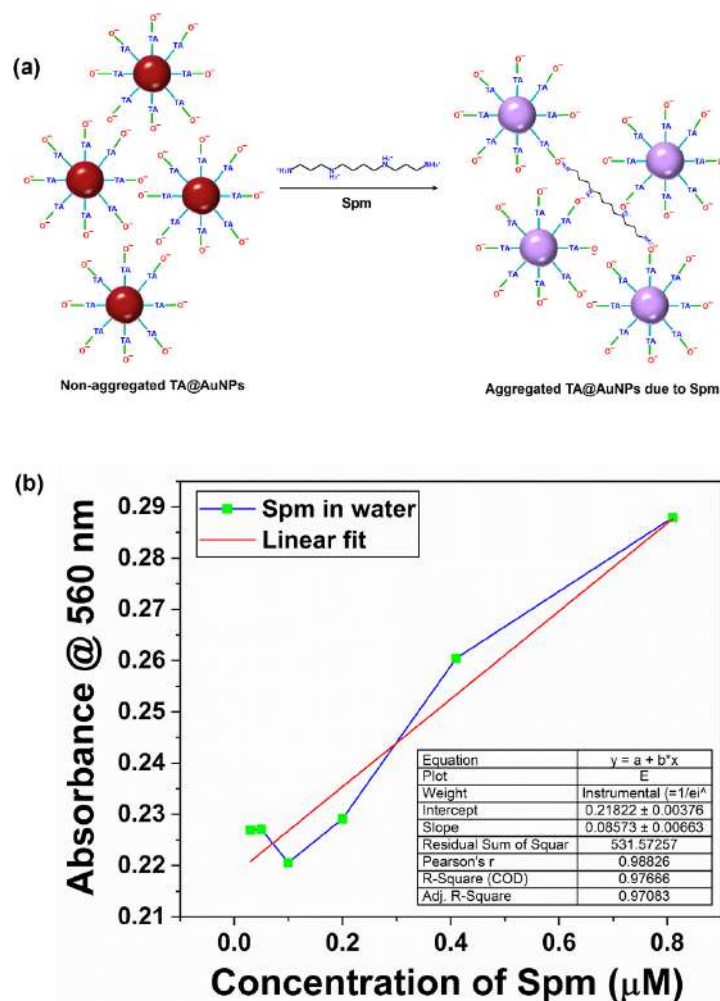


**Figure 6.** (a) Schematic of the sensing process caused by aggregation of TA@AuNPs due to Spm. (b) Graph depicting the absorbance at 560 nm of TA@AuNPs incubated with different concentrations of Spm indicating the sensing process in water.

LOD determination. The LOD was determined from the curve using the mathematical formula mentioned earlier. The LOD of Spd using TA@AuNPs is determined to be a final concentration of 2318 nM [67].

Figure 5(b) shows the change in colour of TA@AuNPs from red to purple on incubation with different concentrations of Spm. This indicates that Spm causes aggregation of TA@AuNPs. This aggregation is depicted as a shift in SPR peak when different concentrations of Spm are incubated with TA@AuNPs in figure 5(c). This aggregation is caused due to electrostatic or hydrogen-bonded interaction of the four amine groups of Spm with the phenolic groups of TA (figure 6(a)). The aggregation of TA@AuNPs is depicted in the graph (figure 5(c)) as a red shift in the SPR peak of TA@AuNPs from 530 nm to higher wavelengths. For LOD determination, a calibration curve (figure 6(b)) was plotted with absorbance values at 560 nm for the same reason as discussed earlier. The LOD was determined using the mathematical equation as mentioned earlier from the curve. The LOD of Spm using TA@AuNPs is determined to be at a final concentration of 145 nM.

Spm sensing was also carried out using PBS as the sensing medium, which influences the colour development process. Figure S13 in the supplementary shows the sensing of Spm using TA@AuNPs as the colourimetric probe when PBS is used as the sensing medium. Since PBS helps in the colour development process during sensing, the LOD of Spm using PBS as the sensing medium is lower than when water was used as the sensing medium. The LOD is determined to be a final concentration of 139 nM from the calibration graph in figure S14 in the supplementary information using the LOD formula mentioned earlier. The ionic strength in PBS is responsible for further accelerating the aggregation process which eventually helps in the colour development process [95]. Thus, when the sensing medium changed from aqueous to PBS an even lower LOD was determined for Spm. For further proof of the aggregation of TA@AuNPs caused by Spm, the nanoparticles were incubated with and without Spm and visualised under TEM. Figures 7(a) and (b) shows the TEM images of the dispersed and aggregated nanoparticles due to Spm, respectively. It was evident that Spm is



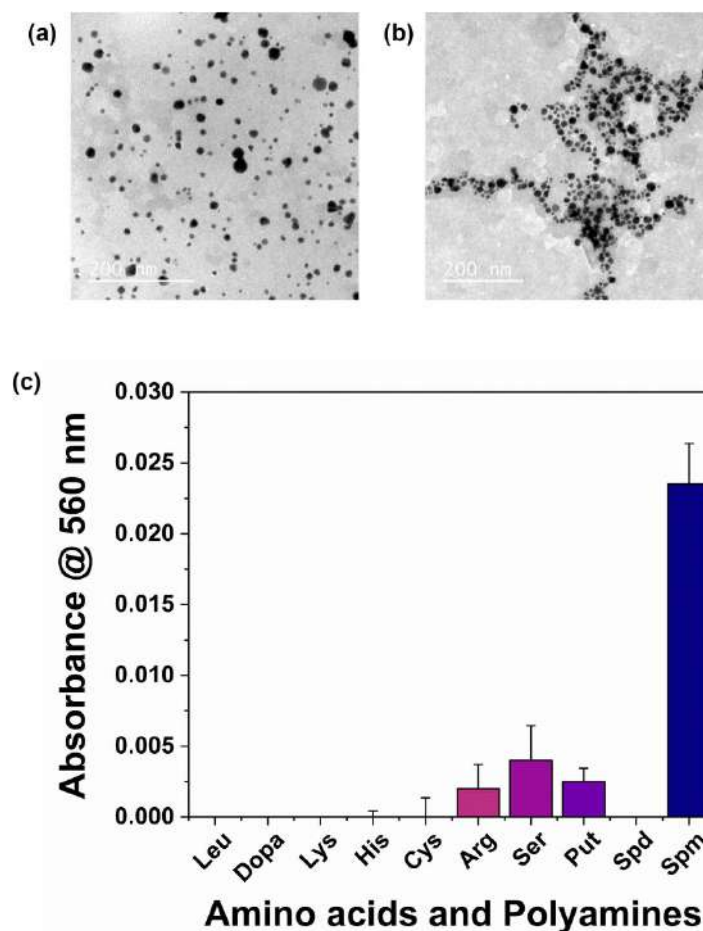


**Figure 7.** (a) TEM image of dispersed TA@AuNPs without Spm. (b) TEM image of aggregated TA@AuNPs incubated with Spm. (c) Bar graph showing the specificity of TA@AuNPs for different amino acids, dopamine, and polyamines.

causing the aggregation of TA@AuNPs. In the absence of the polyamine, the nanoparticles remain dispersed, further supporting that the aggregation was caused by electrostatic interaction between the amine groups of Spm and the phenolic groups of TA (figure 6(a)). The  $pK_a$  value of the amine groups in Spm ranges from 8 to 11 [96]. At physiological pH, polyamines are found to be strongly positively charged and as a result they interact strongly with acidic groups of various macromolecules such as nucleic acids, proteins and phospholipid membranes [53]. Thus, when the sensing medium is deionised water (pH 6.998) or PBS (pH 7.4) the phenolic groups of TA are partially ionised (since  $pK_a$  of TA is 10 as discussed previously) which imparts the nanoparticles with the negative charge. On the other hand, the polyamines in deionised water (pH 6.998) or PBS (pH 7.4) also possess strong positive charges as mentioned above and thus are able to interact electrostatically with the negatively charged TA@AuNPs to cause visible aggregation of the nanoparticles resulting in the shift of the SPR peak.

In conclusion, TA@AuNPs could detect Spd and Spm with a LOD of 2318 nM and 145 nM, respectively. The LOD of Spm was even lower, about 139 nM,

when the sensing was done in PBS. A lower LOD was observed in the case of Spm, possibly because Spm has four amine groups compared to the three amine groups of Spd [71]. As a result, Spm caused more aggregation compared to Spd. Also, the concentration of Spm and Spd in the saliva of OSCC patients is  $16.9 \mu\text{mol ml}^{-1}$  and  $14.7 \mu\text{mol ml}^{-1}$ , respectively [97]. Thus, the LOD for detecting Spm and Spd by TA@AuNPs is much less than the above concentrations. TA@AuNPs did not detect Put. This may be due to the presence of two amine groups in Put, which did not cause sufficient aggregation resulting in colour change. Thus, further experiments were carried out using Spm as the sensitivity of TA@AuNPs was found to be much lower for it compared to Spd.

It was crucial to determine how specific the nanoprobe is in detecting polyamines. In order to determine the specificity of TA@AuNPs, the nanoprobe was incubated with various amino acids and a hormone, dopamine, that might be present in the saliva of the OSCC patients. The absorbance at 560 nm of all the compounds including the polyamines were recorded using a UV-Visible spectrophotometer in triplicates. The absorbance of the blank which consisted of

only the nanoparticle and water instead of any analyte or compound was also recorded. The absorbance was recorded at 560 nm because the SPR peak of TA@AuNPs was found to shift maximum to 560 nm from 530 nm on polyamine detection. The blank absorbance was subtracted from the absorbance of all the other compounds and the polyamines and the resulting absorbances were plotted as a bar graph. Figure 7(c) shows the specificity of TA@AuNPs for polyamine detection. The absorbance value recorded at 560 nm of the amino acids depicted in the graph and the polyamines (Put, Spd and Spm) revealed that TA@AuNPs show very high specificity for Spm at 560 nm. TA@AuNPs exhibited no specificity for amino acids Leu, Lys, His and Cys, or the hormone dopamine, whereas it shows less specificity for Arg, Ser, and the polyamine Put at 560 nm. TA@AuNPs exhibited no specificity for Spd because the concentration considered for determining the specificity of nanoparticles was lower than the LOD of Spd for TA@AuNPs. For most of the compounds the absorbance value was similar to or slightly higher (almost negligible) than the absorbance value of the blank at 560 nm. However, on aggregation of TA@AuNPs by spermine the absorbance value at 560 nm was found to be much higher than the blank because only aggregation of TA@AuNPs can shift the SPR peak to 560 nm resulting in an increase in intensity at 560 nm. Thus, it can be concluded that TA@AuNPs were highly specific for Spm detection among the three polyamines (Put, Spd and Spm). This also signifies that TA@AuNPs cannot detect any compound with less than four amine groups at low concentrations, making it highly specific for Spm. At concentrations higher than the LOD of Spd, TA@AuNPs can also detect Spd. However, Put remained undetected by TA@AuNPs, possibly due to the minimal aggregation caused by the two amine groups of Put even at relatively higher concentrations.

#### 4.4. Nanodrop spectrophotometric and smartphone-based detection of polyamines using TA@AuNPs

TA@AuNPs were incubated with different concentrations of Spd (10, 20, 39, 312, 625, and 1250  $\mu\text{M}$ ) and Spm (39, 52, 156, 312, 625, 1250, and 2500  $\mu\text{M}$ ). The absorbance at 560 nm of each concentration of Spd and Spm was recorded. Figure 8 shows bar graphs depicting the absorbance value at 560 nm of TA@AuNPs incubated with different concentrations of (a) Spd and (b) Spm. The bar graph revealed that with the increase in the concentration of Spd or Spm, the absorbance at 560 nm increases. The  $p$ -value of each concentration of Spd and Spm was determined and compared to the blank that contained only MilliQ water instead of the analyte along with the nanoparticles via one-way ANOVA. Both Spd and

Spm showed increasing significance of  $p$ -value ( $p$ -value  $< 0.0001$ ) with increasing concentrations from 20  $\mu\text{M}$  and 156  $\mu\text{M}$  onwards, respectively. This is because as the concentration of Spd or Spm increased, more nanoparticles became aggregated. As a result, the SPR peak of TA@AuNPs becomes red-shifted; hence, the absorbance at 560 nm increased with increasing concentration.

TA@AuNPs were also incubated with different concentrations of Spd (0.08, 0.15, 0.30, 0.61, 1.22, 2.5, 5, 10, 20, 39, 78, 156, 312.5, 625, 1250, 2500 and 5000  $\mu\text{M}$ ) and Spm (0.08, 0.15, 0.30, 0.61, 1.22, 2.5, 5, 10, 20, 39, 78, 156, 312.5, 625, 1250, 2500 and 5000  $\mu\text{M}$ ) and the RGB values of each were recorded using a smartphone colourimeter app. Among all the concentrations, aggregation was observed from 20  $\mu\text{M}$  onwards for Spd and from 1.22  $\mu\text{M}$  onwards for Spm, depicted by the change in colour of TA@AuNPs from red to purple (figures S15 and S16). The  $R$ -values of each concentration of (a) Spd and (b) Spm is depicted as bar graphs in figure 9. The bar graph (figure 9(a)) reveals that the  $R$ -value decreases with increasing concentration of Spd. Similarly, the bar graph (figure 9(b)) also shows a similar trend like in the case of Spd, i.e. it decreases with increasing concentration of Spm. This indicates that with increasing concentrations of Spd and Spm, the TA@AuNPs aggregates, resulting in the red shift of the SPR peak. As a result, the intensity of red given by TA@AuNPs incubated with each concentration of Spd or Spm decreased with increasing concentrations of the polyamines compared to the  $R$ -value of only the nanoparticles without any polyamine. This further indicates that as the aggregation of the nanoparticle increases with the concentration of the polyamines, the concentration of dispersed nanoparticles in the solution decreases, resulting in a decrease in the  $R$ -value. The  $p$ -value of each set of nanoparticles incubated with different concentrations of Spd and Spm was determined and compared with the blank that contained only deionised water instead of the analyte along with the nanoparticles via one-way ANOVA. TA@AuNPs incubated with different concentrations of Spd showed an increase in significance in  $p$ -value ( $p$ -value  $< 0.0001$ ) compared to the blank from 10  $\mu\text{M}$  onwards. In comparison, TA@AuNPs incubated with different concentrations of Spm showed an increase in significance in  $p$ -value ( $p$ -value  $< 0.0001$ ) compared to the blank from 0.30  $\mu\text{M}$  onwards. Thus, even the smartphone colourimetric app was able to detect much lower concentrations of Spm compared to Spd based on the decrease in the intensity of the  $R$ -value compared to the blank. Thus, the RGB values recorded using a smartphone colourimetric app can be used to detect Spm indirectly using TA@AuNPs as the colourimetric nanoprobe.

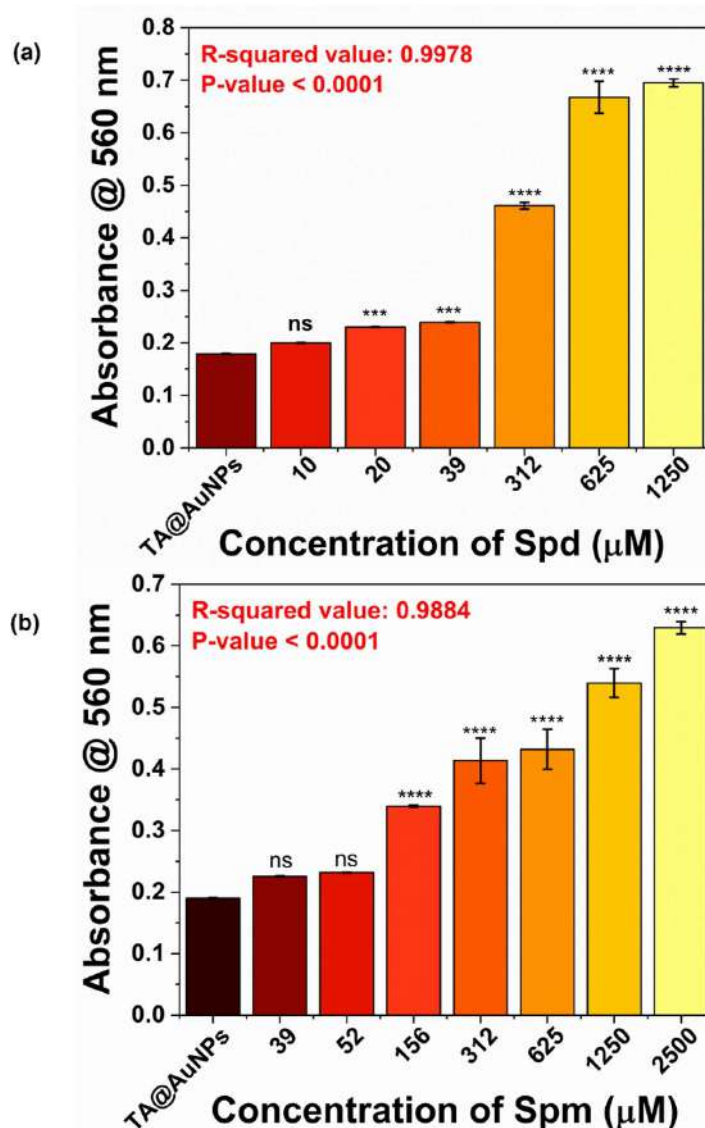


**Figure 8.** (a) Bar graph depicting the absorbance at 560 nm of TA@AuNPs incubated with different concentrations of Spd determined using Nanodrop Spectrophotometer. (b) Bar graph depicting the absorbance at 560 nm of TA@AuNPs incubated with different concentrations of Spm determined using Nanodrop Spectrophotometer. Statistically significant differences at  $*P < 0.01$ ,  $**P < 0.001$ ,  $***P < 0.0001$  were represented with respect to absorbance of blank nanoparticles.

#### 4.5. Colourimetric sensing of polyamines in artificial saliva

It is essential to determine the effect of the artificial saliva on the stability of TA@AuNPs as saliva is a very complex biofluid with many interfering species. TA@AuNPs was added to the artificial saliva and incubated for 15 min before performing a spectral scan to check the position of the SPR peak of the nanoparticles. Figure S17 shows the SPR peak of TA@AuNPs after 15 min incubation in the artificial saliva. The SPR peak was found to be at 530 nm which showed that TA@AuNPs were stable in the artificial saliva. On addition of TA@AuNPs to polyamine spiked artificial saliva samples immediate aggregation of the nanoparticles was observed for higher concentrations of Spm. A spectral scan of the TA@AuNPs incubated with different concentrations of Spm

spiked in artificial saliva is shown in figure 10(a). The SPR peak of TA@AuNPs was redshifted indicating the aggregation of the nanoparticles caused by Spm spiked in the artificial saliva samples. However, no aggregation of the nanoparticles was observed for the blank artificial saliva sample which did not contain any Spm. This further indicates that in the presence of other interfering species in the saliva the nanoparticle showed aggregation only in the presence of Spm emphasising its specificity to the polyamine. The LOD of Spm detection in artificial saliva was determined by plotting a calibration curve (figure 10(b)) using absorbance values recorded at 560 nm using a UV-Visible spectrophotometer as on aggregation of the nanoparticles the SPR peak shifted towards 560 nm from 530 nm and the intensity was found to be higher at 560 nm in comparison to 530 nm.

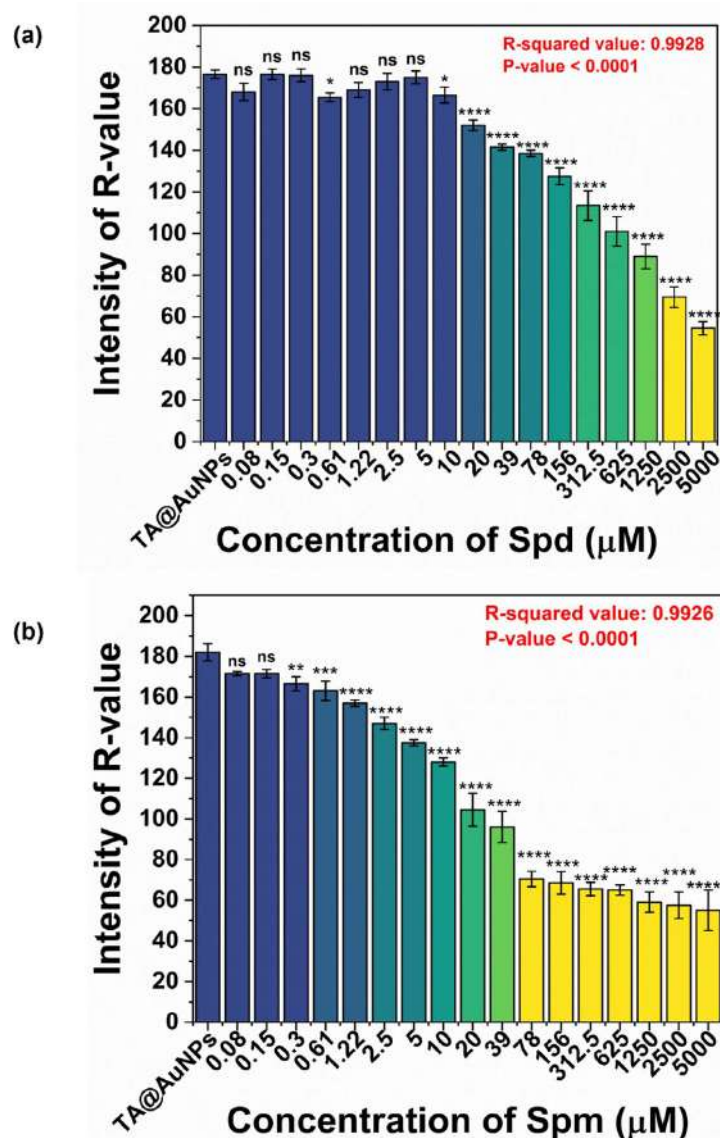


**Figure 9.** (a) Bar graph showing the  $R$ -values of TA@AuNPs incubated with different concentrations of Spd as determined using a colourimetric app. (b) Bar graph showing the  $R$ -values of TA@AuNPs incubated with different concentrations of Spm as determined using a colourimetric app. Statistically significant differences at  $*P < 0.01$ ,  $**P < 0.001$ ,  $***P < 0.0001$  were represented with respect to absorbance of blank nanoparticles.

The LOD was determined using the mathematical equation mentioned earlier and found to be 253 nM. The LODs for Spm sensing using TA@AuNPs has been summarised in table 1.

TA@AuNPs incubated with different concentrations of Spm (13, 26, 52, 104, 208, 417, and 1667  $\mu\text{M}$ ) spiked in artificial saliva were analysed to determine the absorbance at 560 nm. Figure 11(a) shows a bar graph depicting the absorbance value of each set of TA@AuNPs incubated with different concentrations of Spm spiked in artificial saliva. It can be observed from the graph that with increasing concentration of Spm in the artificial saliva there is significant increase in the absorbance at 560 nm. The  $p$ -value for the absorbance at 560 nm for each concentration

was determined using one-way ANOVA and compared with the absorbance of the blank nanoparticles in artificial saliva without any analyte. The  $p$ -value was found to be significant from 13  $\mu\text{M}$  onwards and showed a significant increase for higher concentrations of Spm in artificial saliva ( $p$ -value  $< 0.0001$ ). This indicates that with increasing concentration of Spm in the artificial saliva, more TA@AuNPs aggregated which resulted in the shift of the SPR peak from 530 nm to higher wavelengths, resulting in the sharp increase of absorbance at 560 nm as observed.

TA@AuNPs incubated with different concentrations of Spm (final concentrations of 0.05, 0.1, 0.2, 0.41, 0.81, 1.66, 3.33, 6.66, 13.33, 26, 52, 104.16, 208.33, 416.66, 833.33, 1666.66, and 3333.33  $\mu\text{M}$ )



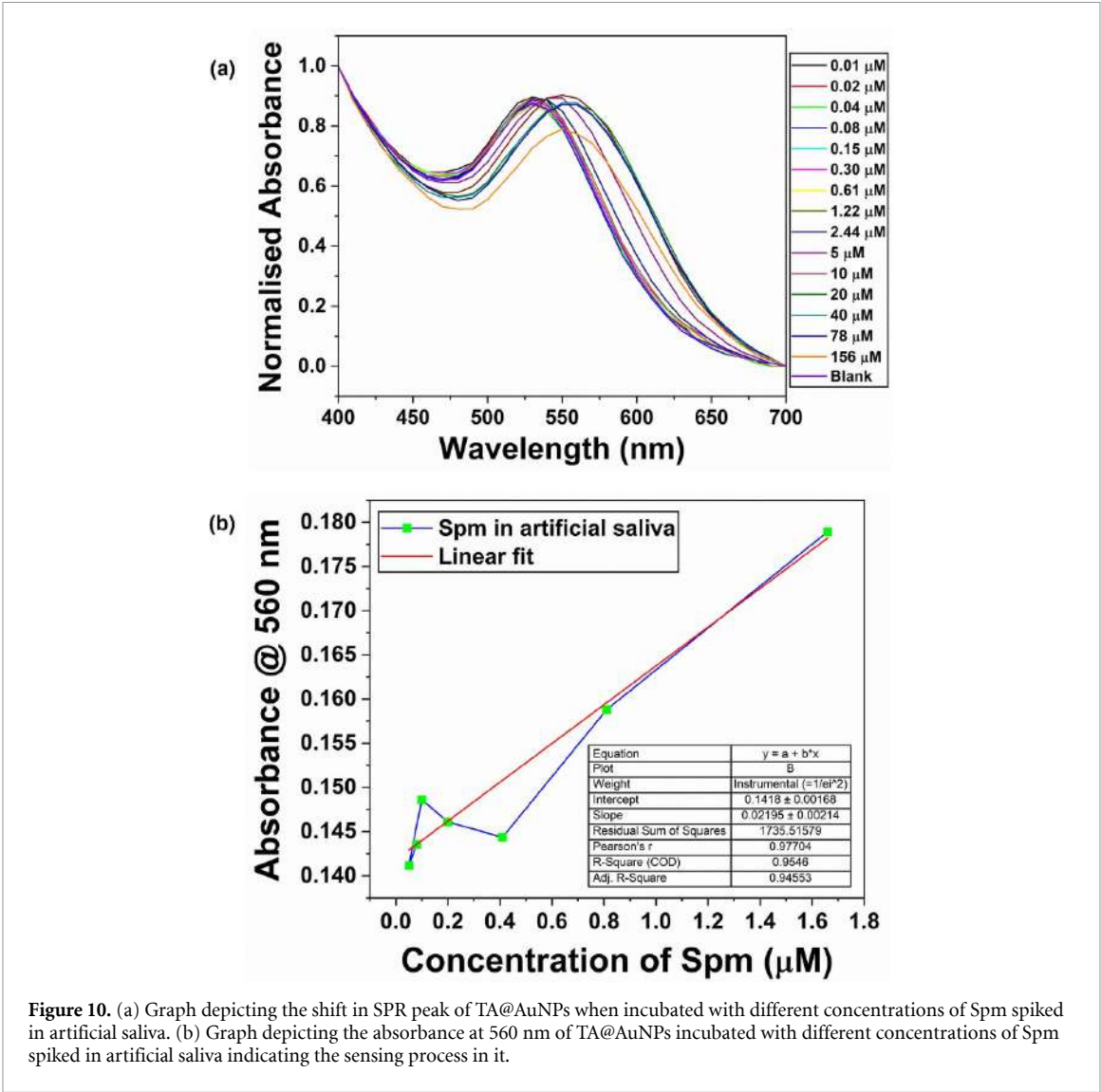


**Figure 10.** (a) Graph depicting the shift in SPR peak of TA@AuNPs when incubated with different concentrations of Spm spiked in artificial saliva. (b) Graph depicting the absorbance at 560 nm of TA@AuNPs incubated with different concentrations of Spm spiked in artificial saliva indicating the sensing process in it.

**Table 1.** Table representing the LODs of Spm sensing in various medium using TA@AuNPs and their concentrations in the saliva of OSCC patients.

Polyamine	LOD <sub>water</sub>	LOD <sub>PBS</sub>	LOD <sub>artificial saliva</sub>	Concentration in saliva of OSCC patients
Spm	145 nM	139 nM	253 nM	16.9 $\mu\text{mol ml}^{-1}$ (16900 nM)

spiked in artificial saliva was analysed using the colourimetric smartphone app. Among all the concentrations of Spm spiked in artificial saliva and incubated with TA@AuNPs, aggregation was observed from 1.66  $\mu\text{M}$  onwards, depicted by the change in colour of TA@AuNPs from red to purple (figure S18). The  $R$ -values were recorded for each set of nanoparticles and a bar graph was plotted. Figure 11(b) shows  $R$ -values of TA@AuNPs incubated with different concentrations of Spm spiked in artificial saliva. From the graph, it can be observed that the  $R$ -value decreases with increasing concentrations of Spm in artificial saliva. This indicates that with increasing concentrations of Spm, more TA@AuNPs aggregate resulting in less number of dispersed TA@AuNPs in solution. As

a result, the red intensity given by the colloidal solution of TA@AuNPs decreases with increasing concentration of Spm in the artificial saliva. The  $p$ -value of each concentration of Spm spiked in artificial saliva was determined using one-way ANOVA and compared to the blank nanoparticles containing only the artificial saliva without any analyte. The  $p$ -value was found to increase significantly from 0.05  $\mu\text{M}$  concentration of Spm in artificial saliva. The average  $p$ -value was determined to be  $p\text{-value} < 0.0001$  which shows that the decrease in  $R$ -value intensity compared to the blank is highly significant. Thus, the colourimetric app was able to detect low concentrations of Spm spiked in artificial saliva with a relevant decrease in the  $R$ -value intensity compared to the blank.

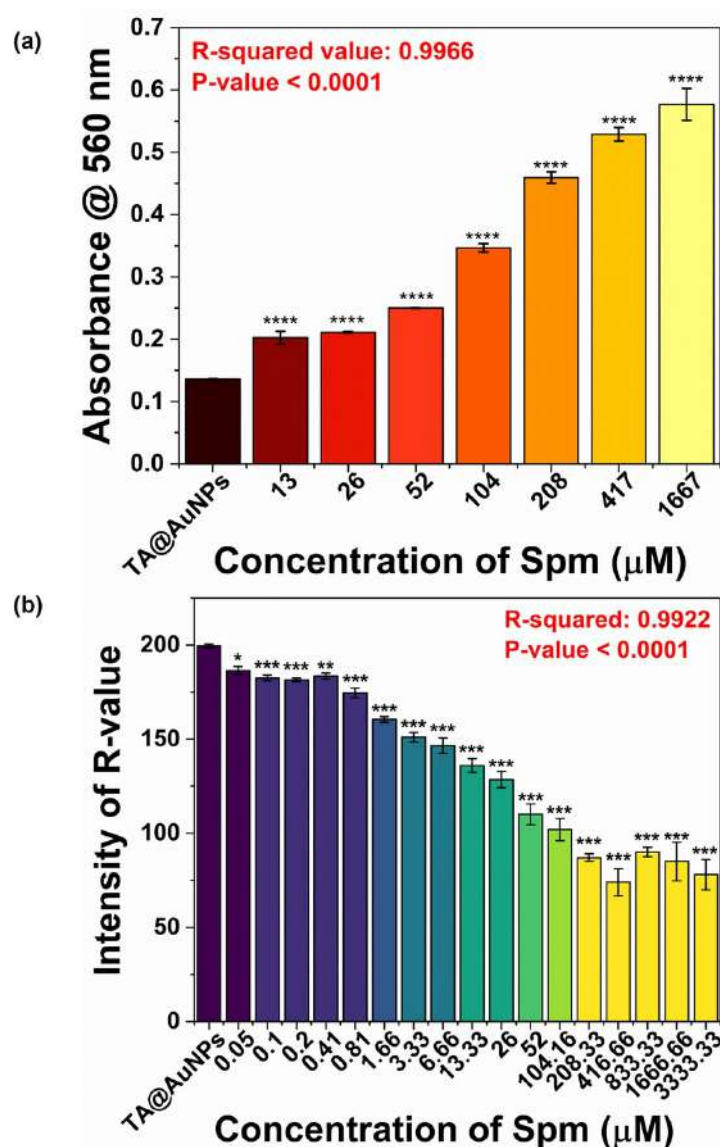


**Figure 11.** (a) Bar graph depicting the absorbance at 560 nm of TA@AuNPs incubated with different concentrations of Spm spiked in artificial saliva determined using Nanodrop Spectrophotometer. (b) Bar graph showing the R-values of TA@AuNPs incubated with different concentrations of Spm spiked in artificial saliva as determined using a colourimetric app. Statistically significant differences at \* $P < 0.01$ , \*\* $P < 0.001$ , \*\*\* $P < 0.0001$  were represented with respect to absorbance of blank nanoparticles.

## 5. Conclusions

Hence, we conclude that TA@AuNPs can be used successfully as a colourimetric nanoprobe to detect Spm. TA@AuNPs showed a significantly lower detection limit for Spm compared to Spd. Hence, the nanoprobe served as a better detector of Spm at lower concentrations. The RGB values recorded using the smartphone colourimeter app provide a convenient method of detection of polyamines using TA@AuNPs. The present study paved the way for the development of an RGB sensor for the sensitive detection using TA@AuNPs, that helps in even lower detection of Spm in the saliva of OSCC patients.

## Data availability statement

The data cannot be made publicly available upon publication because no suitable repository exists for hosting data in this field of study. The data that support the findings of this study are available upon reasonable request from the authors.

## Acknowledgments

The present work has been supported by the *Indian Council of Medical Research-ICRC Task force project under thematic area of 'Diagnostics group'* (No. 5/13/34/GP/ICRC/2022/NCD-III), Government of

India . Asmita Mojumdar and Unnikrishnan B S is grateful to the Ministry of Education (MoE), for the fellowship. The authors are thankful to the Institute Instrumentation Centre (IIC), Centre for Nanotechnology, and Department of Biosciences and Bioengineering, IIT Roorkee, for providing the required infrastructure and various characterization facilities to execute the research work.

## Conflict of interest

Authors declare no conflict of interest.

## Author contributions

**Asmita Mojumdar**- Conceptualization, Methodology, Data curation, Writing- Original draft preparation, and Investigation. **Unnikrishnan B.S.**- Validation and Writing- Reviewing and Editing. **Gopinath Packirisamy**- Validation, Writing- Reviewing and Editing, and Supervision.

## ORCID iDs

Unnikrishnan B S  <https://orcid.org/0000-0002-6885-6409>

Gopinath Packirisamy  <https://orcid.org/0000-0003-1379-1203>

## References

- [1] Boring C C, Squires T S and Tong T 1992 Cancer statistics, 1992 *CA A Cancer J. Clin.* **42** 19–38
- [2] Mascitti M, Orsini G, Tosco V, Monterubbiansi R, Balercia A, Putignano A, Procaccini M and Santarelli A 2018 An overview on current non-invasive diagnostic devices in oral oncology *Front. Physiol.* **9** 1510
- [3] Ram H, Sarkar J, Kumar H, Konwar R, Bhatt M L B and Mohammad S 2011 Oral Cancer: risk Factors and Molecular Pathogenesis *J. Maxillofacial Oral Surg.* **10** 132–7
- [4] Herceg Z and Hainaut P 2007 Genetic and epigenetic alterations as biomarkers for cancer detection, diagnosis and prognosis *Mol. Oncol.* **1** 26–41
- [5] Mishra A and Verma M 2010 Cancer Biomarkers: are We Ready for the Prime Time? *Cancers* **2** 190–208
- [6] Nass S J and Moses H L (eds) 2007 *Cancer Biomarkers: The Promises and Challenges of Improving Detection and Treatment* (National Academies Press) (available at: [www.nap.edu/catalog/11892](http://www.nap.edu/catalog/11892))
- [7] Kalkal A, Pradhan R, Kadian S, Manik G and Packirisamy G 2020 Biofunctionalized graphene quantum dots based fluorescent biosensor toward efficient detection of small cell lung cancer *ACS Appl. Bio Mater.* **3** 4922–32
- [8] Henry N L and Hayes D F 2012 Cancer biomarkers *Mol. Oncol.* **6** 140–6
- [9] Cheng Y S L, Rees T and Wright J 2014 A review of research on salivary biomarkers for oral cancer detection *Clin. Transl. Med.* **3** 3
- [10] Neville B W and Day T A 2002 Oral cancer and precancerous lesions *CA: A Cancer J. Clin.* **52** 195–215
- [11] Hofman L F 2001 Human saliva as a diagnostic specimen *J. Nutrition* **131** 1621S–5S
- [12] Lima D P, Diniz D G, Moimaz S A S, Sumida D H and Okamoto A C 2010 Saliva: reflection of the body *Int. J. Infect. Dis.* **14** e184–188
- [13] Malathi N, Mythili S and Vasanthi H R 2014 Salivary diagnostics: a brief review *ISRN Dent.* **2014** 158786
- [14] Deepa T and Thirrunavukkarasu N 2010 Saliva as a potential diagnostic tool *Indian J. Med. Sci.* **64** 293–306
- [15] Kaufman E and Lamster I B 2002 The diagnostic applications of saliva—a review *Crit. Rev. Oral Biol. Med.* **13** 197–212
- [16] Nagler R, Bahar G, Shpitzer T and Feinmesser R 2006 Concomitant analysis of salivary tumor markers—a new diagnostic tool for oral cancer *Clin. Cancer Res.* **12** 3979–84
- [17] Santosh A B R, Jones T and Harvey J 2016 A review on oral cancer biomarkers: understanding the past and learning from the present *J. Cancer Res. Ther.* **12** 486–92
- [18] Mikkonen J J W, Singh S P, Herrala M, Lappalainen R, Myllymaa S and Kullaa A M 2016 Salivary metabolomics in the diagnosis of oral cancer and periodontal diseases *J. Periodontal Res.* **51** 431–7
- [19] Singh P, Verma J K and Singh J K 2020 Validation of salivary markers, IL-1 $\beta$ , IL-8 and Lgals3bp for detection of oral squamous cell carcinoma in an indian population *Sci. Rep.* **10** 7365
- [20] Clayton T A et al 2006 Pharmaco-metabonomic phenotyping and personalized drug treatment *Nature* **440** 1073–7
- [21] Fiehn O 2002 Metabolomics—the link between genotypes and phenotypes *Plant Mol. Biol.* **48** 155–71
- [22] Holmes E, Wilson I D and Nicholson J K 2008 Metabolic phenotyping in health and disease *Cell* **134** 714–7
- [23] Chicharro J L, Lucía A, Pérez M, Vaquero A F and Ureña R 1998 Saliva composition and exercise *Sports Med.* **26** 17–27
- [24] Bigler L R, Streckfus C F and Dubinsky W P 2009 Salivary biomarkers for the detection of malignant tumors that are remote from the oral cavity *Clin. Lab. Med.* **29** 71–85
- [25] Samaranayake L 2007 Saliva as a diagnostic fluid *Int. Dent. J.* **57** 295–9
- [26] Wong D T 2006 Towards a simple, saliva-based test for the detection of oral cancer ‘oral fluid (saliva), which is the mirror of the body, is a perfect medium to be explored for health and disease surveillance *Expert Rev. Mol. Diagn.* **6** 267–72
- [27] Humphrey S P and Williamson R T 2001 A review of saliva: normal composition, flow, and function *J. Prosthet. Dent.* **85** 162–9
- [28] Ohshima M, Sugahara K, Kasahara K and Katakura A 2017 Metabolomic analysis of the saliva of Japanese patients with oral squamous cell carcinoma *Oncol. Rep.* **37** 2727–34
- [29] Lohavanichbutr P, Zhang Y, Wang P, Gu H, Nagana Gowda G A, Djukovic D, Buas M F, Raftery D and Chen C 2018 Salivary metabolite profiling distinguishes patients with oral cavity squamous cell carcinoma from normal controls *PLoS One* **13** e0204249
- [30] Sridharan G, Ramani P and Patankar S 2017 Serum metabolomics in oral leukoplakia and oral squamous cell carcinoma *J. Cancer Res. Ther.* **13** 556–61
- [31] Awasthi N 2017 Role of salivary biomarkers in early detection of oral squamous cell carcinoma *Indian J. Pathol. Microbiol.* **60** 464–8
- [32] Mukherjee P K, Funchain P, Retuerto M, Jurevic R J, Fowler N, Burkey B, Eng C and Ghannoum M A 2017 Metabolomic analysis identifies differentially produced oral metabolites, including the oncometabolite 2-hydroxyglutarate, in patients with head and neck squamous cell carcinoma *BBA Clin.* **7** 8–15
- [33] Nguyen T T H, Sodnom-Ish B, Choi S W, Jung H I, Cho J, Hwang I and Kim S M 2020 Salivary biomarkers in oral squamous cell carcinoma *J. Korean Assoc. Oral Maxillofac. Surg.* **46** 301–12
- [34] Bel'skaya L V, Sarf E A, Solomatin D V and Kosenok V K 2020 Diagnostic and prognostic value of salivary biochemical markers in oral squamous cell carcinoma *Diagnostics* **10** 818
- [35] Ishikawa S, Wong D T W, Sugimoto M, Gleber-Netto F O, Li F, Tu M, Zhang Y, Akin D and Iino M 2019 Identification of salivary metabolites for oral squamous cell carcinoma and

- oral epithelial dysplasia screening from persistent suspicious oral mucosal lesions *Clin. Oral Investig.* **23** 3557–63
- [36] Ishikawa S et al 2016 Identification of salivary metabolomic biomarkers for oral cancer screening *Sci. Rep.* **6** 31520
- [37] Ishikawa S, Sugimoto M, Edamatsu K, Sugano A, Kitabatake K and Iino M 2020 Discrimination of oral squamous cell carcinoma from oral lichen planus by salivary metabolomics *Oral Dis.* **26** 35–42
- [38] Song X, Yang X, Narayanan R, Shankar V, Ethiraj S, Wang X, Duan N, Ni Y-H, Hu Q and Zare R N 2020 Oral squamous cell carcinoma diagnosed from saliva metabolic profiling *Proc. Natl Acad. Sci. USA* **117** 16167–73
- [39] Sugimoto M, Wong D T, Hirayama A, Soga T and Tomita M 2010 Capillary electrophoresis mass spectrometry-based saliva metabolomics identified oral, breast and pancreatic cancer-specific profiles *Metabolomics* **6** 78–95
- [40] Wang Q, Gao P, Cheng F, Wang X and Duan Y 2014 Measurement of salivary metabolite biomarkers for early monitoring of oral cancer with ultra performance liquid chromatography-mass spectrometry *Talanta* **119** 299–305
- [41] Wang J, Christison T T, Misuno K, Lopez L, Huhmer A F, Huang Y and Hu S 2014 Metabolomic profiling of anionic metabolites in head and neck cancer cells by capillary ion chromatography with Orbitrap mass spectrometry *Anal. Chem.* **86** 5116–24
- [42] Wang Q, Gao P, Wang X and Duan Y 2014 The early diagnosis and monitoring of squamous cell carcinoma via saliva metabolomics *Sci. Rep.* **4** 6802
- [43] Wei J, Xie G, Zhou Z, Shi P, Qiu Y, Zheng X, Chen T, Su M, Zhao A and Jia W 2011 Salivary metabolite signatures of oral cancer and leukoplakia *Int. J. Cancer* **129** 2207–17
- [44] Gardner A, Parkes H G, So P W and Carpenter G H 2019 Determining bacterial and host contributions to the human salivary metabolome *J. Oral Microbiol.* **11** 1617014
- [45] Kirwan J A, Brennan L, Broadhurst D, Fiehn O, Cascante M, Dunn W B, Schmidt M A and Velagapudi V 2018 Preanalytical processing and biobanking procedures of biological samples for metabolomics research: a white paper, community perspective (for ‘precision medicine and pharmacometabolomics task group’-the metabolomics society initiative) *Clin. Chem.* **64** 1158–82
- [46] Liebsch C et al 2019 The saliva metabolome in association to oral health status *J. Dent. Res.* **98** 642–51
- [47] Takeda I, Stretch C, Barnaby P, Bhatnager K, Rankin K, Fu H, Weljie A, Jha N and Slupsky C 2009 Understanding the human salivary metabolome *NMR Biomed.* **22** 577–84
- [48] Tabor C W and Tabor H 1984 Polyamines *Annu. Rev. Biochem.* **53** 749–90
- [49] Igarashi K and Kashiwagi K 2010 Modulation of cellular function by polyamines *Int. J. Biochem. Cell Biol.* **42** 39–51
- [50] Pegg A E and Casero R A 2011 Current status of the polyamine research field *Methods Mol. Biol.* **720** 3–35
- [51] Bachrach U 2005 Naturally occurring polyamines: interaction with macromolecules *Curr. Protein Peptide Sci.* **6** 559–66
- [52] Park M H and Igarashi K 2013 Polyamines and their metabolites as diagnostic markers of human diseases *Biomol. Ther.* **21** 1–9
- [53] Pegg A E 2009 Mammalian polyamine metabolism and function *IUBMB Life* **61** 880–94
- [54] Clarke R A, Schirra H J, Catto J W, Lavin M F and Gardiner R A 2010 Markers for detection of prostate cancer *Cancers* **2** 1125–54
- [55] de Sá Alves M et al 2021 Identification of possible salivary metabolic biomarkers and altered metabolic pathways in south american patients diagnosed with oral squamous cell carcinoma *Metabolites* **11** 650
- [56] Niitsu M, Samejima K, Matsuzaki S and Hamana K 1993 Systematic analysis of naturally occurring linear and branched polyamines by gas chromatography and gas chromatography—mass spectrometry *J. Chromatogr. A* **641** 115–23
- [57] Rawat K A, Bhamore J R, Singhal R K and Kailasa S K 2017 Microwave assisted synthesis of tyrosine protected gold nanoparticles for dual (colorimetric and fluorimetric) detection of spermine and spermidine in biological samples *Biosens. Bioelectron.* **88** 71–77
- [58] Satrijo A and Swager T M 2007 Anthryl-doped conjugated polyelectrolytes as aggregation-based sensors for nonquenching multicationic analytes *J. Am. Chem. Soc.* **129** 16020–8
- [59] Lee B, Scopelliti R and Severin K 2011 A molecular probe for the optical detection of biogenic amines *Chem. Commun.* **47** 9639–41
- [60] Köstereli Z and Severin K 2012 Fluorescence sensing of spermine with a frustrated amphiphile *Chem. Commun.* **48** 5841–3
- [61] Chow C F, Lam M H W and Wong W Y 2013 Design and synthesis of heterobimetallic Ru(II)–Ln(III) complexes as chemodosimetric ensembles for the detection of biogenic amine odorants *Anal. Chem.* **85** 8246–53
- [62] Fletcher J T and Bruck B S 2015 Spermine detection via metal-mediated ethynylarene ‘turn-on’ fluorescence signaling *Sens. Actuators B* **207** 843–8
- [63] Tanima D, Imamura Y, Kawabata T and Tsubaki K 2009 Development of highly sensitive and selective molecules for detection of spermidine and spermine *Org. Biomol. Chem.* **7** 4689–94
- [64] Tummala R, Diegelman P, Fiuza S M, Batista de Carvalho L A E, Marques M P M, Kramer D L, Clark K, Vujcic S, Porter C W and Pendyala L 2010 Characterization of Pt-, Pd-spermine complexes for their effect on polyamine pathway and cisplatin resistance in A2780 ovarian carcinoma cells *Oncol. Rep.* **24** 15–24
- [65] Piermarini S, Volpe G, Federico R, Moscone D and Palleschi G 2010 Detection of biogenic amines in human saliva using a screen-printed biosensor *Anal. Lett.* **43** 1310–6
- [66] Cheng Y, Jiang P and Dong X 2015 Molecularly imprinted fluorescent chemosensor synthesized using quinoline-modified- $\beta$ -cyclodextrin as monomer for spermidine recognition *RSC Adv.* **5** 55066–74
- [67] Chopra S, Singh J, Kaur H, Singh H, Singh N and Kaur N 2015 Selective chemosensing of spermidine based on fluorescent organic nanoparticles in aqueous media via a Fe<sup>3+</sup> displacement assay *New J. Chem.* **39** 3507–12
- [68] Chopra S, Singh A, Venugopalan P, Singh N and Kaur N 2017 Organic nanoparticles for visual detection of spermidine and spermine in vapors and aqueous phase *ACS Sustain. Chem. Eng.* **5** 1287–96
- [69] Fukushima Y and Aikawa S 2019 Colorimetric detection of spermine and spermidine by zincon in aqueous solution *Tetrahedron Lett.* **60** 151302
- [70] Shkodra B, Petrelli M, Costa Angeli M, Sarwar Inam A, Avancini E, Münzenrieder N, Lugli P and Petti L 2021 Flexible carbon nanotube-based electrolyte-gated field-effect transistor for spermidine detection 2021 *IEEE Int. Conf. on Flexible and Printable Sensors and Systems (FLEPS)* pp 1–4
- [71] Abbasi-Moayed S, Bigdeli A and Hormozi-Nezhad M R 2022 Determination of spermine and spermidine in meat with a ratiometric fluorescence nanoprobe and a combinational logic gate *Food Chem.* **384** 132459
- [72] Saha K, Agasti S S, Kim C, Li X and Rotello V M 2012 Gold nanoparticles in chemical and biological sensing *Chem. Rev.* **112** 2739–79
- [73] Dykman L A and Khlebtsov N G 2014 Uptake of engineered gold nanoparticles into mammalian cells *Chem. Rev.* **114** 1258–88
- [74] Zhou W, Gao X, Liu D and Chen X 2015 Gold nanoparticles for *in vitro* diagnostics *Chem. Rev.* **115** 10575–636
- [75] Yeh Y-C, Creran B and Rotello V M 2012 Gold nanoparticles: preparation, properties, and applications in bionanotechnology *Nanoscale* **4** 1871–80
- [76] Kalkal A, Pradhan R and Packirisamy G 2023 Gold nanoparticles modified reduced graphene oxide nanosheets



- based dual-quencher for highly sensitive detection of carcinoembryonic antigen *Int. J. Biol. Macromol.* **242** 125157
- [77] Gülçin İ, Huyut Z, Elmastaş M and Aboul-Enein H Y 2010 Radical scavenging and antioxidant activity of tannic acid *Arab. J. Chem.* **3** 43–53
- [78] Chen S-C and Chung K-T 2000 Mutagenicity and antimutagenicity studies of tannic acid and its related compounds *Food Chem. Toxicol.* **38** 1–5
- [79] Vance R E and Teel R W 1989 Effect of tannic acid on rat liver S9 mediated mutagenesis, metabolism and DNA binding of benzo[a]pyrene *Cancer Lett.* **47** 37–44
- [80] Khan W A, Wang Z Y, Athar M, Bickers D R and Mukhtar H 1988 Inhibition of the skin tumorigenicity of (±)-7β,8α-dihydroxy-9α,10α-epoxy-7,8,9,10-tetrahydrobenzo[a]pyrene by tannic acid, green tea polyphenols and quercetin in senar mice *Cancer Lett.* **42** 7–12
- [81] Serebrennikova K V, Komova N S, Berlina A N, Zherdev A V and Dzantiev B B 2021 Tannic acid-capped gold nanoparticles as a novel nanozyme for colorimetric determination of Pb<sup>2+</sup> ions *Chemosensors* **9** 332
- [82] Suherman A L, Zampardi G, Amin H M A, Young N P and Compton R G 2019 Tannic acid capped gold nanoparticles: capping agent chemistry controls the redox activity *Phys. Chem. Chem. Phys.* **21** 4444–51
- [83] Joint Research Centre (European Commission), Robouch P, Stroka J, Haedrich J, Schaechtele A and Wenzl T 2016 *Guidance document on the estimation of LOD and LOQ for measurements in the field of contaminants in feed and food* (Publications Office of the European Union) (available at: <https://data.europa.eu/doi/10.2787/8931>) Accessed 26 December 2023
- [84] Aswathy Aromal S and Philip D 2012 Facile one-pot synthesis of gold nanoparticles using tannic acid and its application in catalysis *Physica E* **44** 1692–6
- [85] Lopes L C S, Brito L M, Bezerra T T, Gomes K N, Fada C and Chaves M H, Cantanhede W 2018 Silver and gold nanoparticles from tannic acid: synthesis, characterization and evaluation of antileishmanial and cytotoxic activities *An. Acad. Bras. Ciênc.* **90** 2679–89
- [86] Ahmad T 2014 Reviewing the tannic acid mediated synthesis of metal nanoparticles *J. Nanotechnol.* **2014** 1–11
- [87] Huang X, Devi S, Bordiga M, Brennan C S and Xu B 2023 Phenolic compounds mediated biosynthesis of gold nanoparticles and evaluation of their bioactivities: a review *Int. J. Food Sci. Technol.* **58** 1673–94
- [88] Amini S M and Akbari A 2019 Metal nanoparticles synthesis through natural phenolic acids *IET Nanobiotechnol.* **13** 771–7
- [89] Cerezo-Navarrete C, David A H, García-Zaragoza A, Codesal M D, Oña-Burgos P, Del Rosal I, Poteau R, Campaña A G and Martínez-Prieto L M 2022 Ruthenium nanoparticles canopied by heptagon-containing saddle-shaped nanographenes as efficient aromatic hydrogenation catalysts *Chem. Sci.* **13** 13046–59
- [90] Bezuneh T T, Ofgea N M, Tessema S S and Bushira F A 2023 Tannic acid-functionalized silver nanoparticles as colorimetric probe for the simultaneous and sensitive detection of aluminum (III) and fluoride ions *ACS Omega* **8** 37293–301
- [91] Baliga S, Muglikar S and Kale R 2013 Salivary pH: a diagnostic biomarker *J. Indian. Soc. Periodontol.* **17** 461–5
- [92] Ramya A S, Uppala D, Majumdar S, Surekha C and Deepak K G K 2015 Are salivary amylase and pH—Prognostic indicators of cancers? *J. Oral Biol. Craniofac. Res.* **5** 81–85
- [93] Iorgulescu G 2009 Saliva between normal and pathological. Important factors in determining systemic and oral health *J. Med. Life* **2** 303–7
- [94] Jenzano J W, Hogan S L and Lundblad R L 1986 Factors influencing measurement of human salivary lysozyme in lysoplate and turbidimetric assays *J. Clin. Microbiol.* **24** 963–7
- [95] Du S, Kendall K, Toloueinia P, Mehrabadi Y, Gupta G and Newton J 2012 Aggregation and adhesion of gold nanoparticles in phosphate buffered saline *J. Nanopart. Res.* **14** 758
- [96] Blagbrough I S, Metwally A A and Geall A J 2011 Measurement of polyamine pKa Values *Polyamines: Methods and Protocols (Methods in Molecular Biology)* ed A E Pegg and R A Casero Jr (Humana Press) pp 493–503
- [97] Gaphor S 2010 Relationship between interleukine-1 alpha and polyamines levels in serum and saliva as potential biomarkers in the diagnosis of oral squamous cell carcinoma *J. Baghdad Coll. Dent.* **22** 50–54



# Ti<sub>3</sub>C<sub>2</sub>-MXene decorated with nanostructured silver as a dual-energy acceptor for the fluorometric neuron specific enolase detection

Ashish Kalkal<sup>a</sup>, Sachin Kadian<sup>b</sup>, Sumit Kumar<sup>c</sup>, Gaurav Manik<sup>b</sup>, Prosenjit Sen<sup>d</sup>, Saurabh Kumar<sup>d,e,\*\*</sup>, Gopinath Packirisamy<sup>a,f,\*</sup>

<sup>a</sup> Nanobiotechnology Laboratory, Department of Biosciences and Bioengineering, Indian Institute of Technology Roorkee, Uttarakhand, 247667, India

<sup>b</sup> Department of Polymer and Process Engineering, Indian Institute of Technology Roorkee, Uttarakhand, 247667, India

<sup>c</sup> Department of Research and Innovations, Division of Research and Development, Lovely Professional University, Jalandhar, Punjab, 144411, India

<sup>d</sup> Centre for Nano Science and Engineering (CeNSE), Indian Institute of Science Bengaluru, Karnataka, 560012, India

<sup>e</sup> Department of Medical Devices, National Institute of Pharmaceutical Education and Research Guwahati, Assam, 781101, India

<sup>f</sup> Centre for Nanotechnology, Indian Institute of Technology Roorkee, Uttarakhand, 247667, India

## ARTICLE INFO

### Keywords:

Energy transfer  
Ti<sub>3</sub>C<sub>2</sub>-MXene  
Graphene quantum dots (GQDs)  
Fluorescent biosensor  
Neuron-specific enolase (NSE)

## ABSTRACT

Nanohybrids of two-dimensional (2D) layered materials have shown fascinating prospects towards the fabrication of highly efficient fluorescent immunosensor. In this context, a nanohybrid of ultrathin Ti<sub>3</sub>C<sub>2</sub>-MXene nanosheets and silver nanoparticles (Ag@Ti<sub>3</sub>C<sub>2</sub>-MXene) has been reported as a dual-energy acceptor for ultra-high fluorescence quenching of protein-functionalized graphene quantum dots (anti-NSE/amino-GQDs). The Ti<sub>3</sub>C<sub>2</sub>-MXene nanosheets are decorated with silver nanoparticles (AgNPs) to obsolete the agglomeration and restacking through a one-pot direct reduction method wherein the 2D Ti<sub>3</sub>C<sub>2</sub>-MXene nanosheets acted both as a reducing agent and support matrix for AgNPs. The as-prepared nanohybrid is characterized by various techniques to analyze the optical, structural, compositional, and morphological parameters. The quenching efficiency and energy transfer capability between the anti-NSE/amino-GQDs (donor) and Ag@Ti<sub>3</sub>C<sub>2</sub>-MXene (acceptor) have been explored through steady state and time-resolved spectroscopic studies. Interestingly, the Ag@Ti<sub>3</sub>C<sub>2</sub>-MXene nanohybrid exhibits better quenching and energy transfer efficiencies in contrast to bare Ti<sub>3</sub>C<sub>2</sub>-MXene, AgNPs and previously reported AuNPs. Based on optimized donor-acceptor pair, a fluorescent turn-on biosensing system is constructed that revealed improved biosensing characteristics compared to Ti<sub>3</sub>C<sub>2</sub>-MXene, graphene and AuNPs for the detection of neuron-specific enolase (NSE), including higher sensitivity (~771 mL ng<sup>-1</sup>), broader linear detection range (0.0001–1500 ng mL<sup>-1</sup>), better LOD (0.05 pg mL<sup>-1</sup>), and faster response time (12 min). Besides, remarkable biosensing capability has been observed in serum samples, with fluorescence recovery of ~98%.

## 1. Introduction

A rapid accession in the exploration of zero-dimensional (0D) and two-dimensional (2D) based nanohybrid materials comprising derivatives of graphene, metal nanoparticles, transition metal oxides, dichalcogenides, including carbides, nitrides, and carbonitrides has shown a multifold rise in the field of bio and nanoelectronics engineering (Anasori et al., 2017; Chauhan et al., 2020; Kalkal et al., 2021c; Kumar et al. 2016, 2018a, Kumar et al., 2019a; Liu et al., 2017; Peng et al., 2016). These advanced materials possess exceptional optical,

mechanical, electronic, and physicochemical properties. Owing to these properties, their utilization has shown a well-proven scope in plenty of applications, especially energy conversion (Kumar et al., 2019b; Sun et al., 2017), supercapacitor (Zhou et al., 2020), biomedical (Huang et al., 2018), water purification (Pandey et al., 2018), and biosensing (Kumar et al., 2018a; Pradhan et al., 2021a). Moreover, in the last decade, 2D layered materials delivered an extraordinary impact in the field of fluorescent biosensors, wherein efficient donor-acceptor pairs are being explored to obtain enhanced energy transfer rates in view of achieving improved analytical performance (Neema et al., 2020; Peng

\* Corresponding author. Nanobiotechnology Laboratory, Department of Biosciences and Bioengineering, Indian Institute of Technology Roorkee, Uttarakhand, 247667, India.

\*\* Corresponding author. Centre for Nano Science and Engineering (CeNSE), Indian Institute of Science Bengaluru, Karnataka, 560012, India.

E-mail addresses: [sau2203@gmail.com](mailto:sau2203@gmail.com) (S. Kumar), [genegopi@gmail.com](mailto:genegopi@gmail.com), [gopi@bt.iitr.ac.in](mailto:gopi@bt.iitr.ac.in) (G. Packirisamy).

<https://doi.org/10.1016/j.bios.2021.113620>

Received 27 May 2021; Received in revised form 18 August 2021; Accepted 6 September 2021

Available online 16 September 2021

0956-5663/© 2021 Elsevier B.V. All rights reserved.

et al., 2019; Tian et al., 2017; Zhu et al., 2019).

In this direction, quantum dots, including molybdenum disulfide ( $\text{MoS}_2$ ), carbon dots (CDs), graphene quantum dots (GQDs), etc., have immensely evolved as energy donor species due to their unusual optical and electronic properties (Bhatnagar et al., 2016; Kadian et al., 2019; Kalkal et al., 2021a; Shao et al., 2019; Swaminathan et al., 2017). These quantum dots provide good biocompatibility, broad excitation spectra, good water solubility, tunable emission spectra, and intense fluorescence with long-term photostability (Kalkal et al., 2020, 2021b). On the other hand, 0D and 2D nanomaterials, including metal nanoparticles (gold and silver nanoparticles (Au and Ag NPs), graphene and its derivatives (reduced graphene oxide (RGO), graphene oxide (GO)) have been deployed as energy acceptor species in the development of fluorescent biosensors (Ghosh and Chattopadhyay, 2015; Neema et al., 2020). Conforming to this, Amjadi et al. demonstrated the fluorescent turn-on sensing probe for the detection of cysteine that utilizes CDs and AgNPs as donor-acceptor pair (Amjadi et al., 2015). In our previous work, we recently reported the development of a fluorescent biosensor for NSE detection based on AuNPs and amine-functionalized nitrogen-doped GQDs (Kalkal et al., 2020). Conversely, Bhatnagar et al. fabricated an immunosensor utilizing GQDs and graphene as energy donor-acceptor pair for detecting cardiac troponin I (CTnI) biomarker. (Bhatnagar et al., 2016).

However, it has been predicted that dispersed metal nanoparticles may tend to agglomerate in solution due to the Brownian motion of suspended nanoparticles, forming larger clusters having a smaller surface area that may inhibit the energy transfer efficiency and quenching capabilities (Mahdavi et al., 2019; Tilaki et al., 2006). Besides, 2D layered nanomaterials have a tendency to restack due to strong van der Waals forces between the adjacent nanosheets that may further influence the biosensing parameters (Atif and Inam, 2016; Cha et al., 2016; He et al., 2019). These problems might be overcome by preparing a 0D and 2D-based nanohybrid material that can work as a dual-energy acceptor and facilitate in improving the energy transfer efficiency along with biosensing parameters. In that, 2D layered nanomaterial can help in inhibiting the Brownian motion of metal nanoparticles by acting as a support matrix, thereby avoiding the inherent agglomeration. Additionally, the restacking among the 2D nanosheets can be inhibited by incorporating the 0D nanoparticles that help in generating the interlayer spacing among layered nanosheets (Kalali et al., 2020; Torres-Mendieta et al., 2016). In this context, Kumar et al. utilized the RGO nanosheets as the support matrix to reduce the agglomeration by inhibiting the Brownian motion of nanostructured metal oxide. The resultant nanohybrid-based sensing platform exhibited superior biosensing parameters, including higher sensitivity and broader linear detection range (Kumar et al., 2018a; Kumar and Kalkal, 2021). However, in case of graphene-based 2D nanomaterials, the decoration of 0D nanomaterials can occur only on edge and defect sites of graphene nanosheets (Bellunato et al., 2016; Vedala et al., 2011). Besides, chemically synthesized graphene (RGO) requires an additional reducing agent for *in-situ* decoration or an additional step for *ex-situ* decoration of 0D nanomaterial on RGO nanosheets (Cui et al., 2013; Ikram et al., 2020; Su et al., 2018). Moreover, the conventional graphene-based 2D layered nanomaterials possess low-hydrophilicity, inadequate surface terminated functionality, difficulty in functionalization that may influence the intrinsic properties and fluorescent biosensing applications of graphene-based layered materials.

In the view of foregoing, a new and emerging material named MXene having the general formula of  $\text{M}_{n+1}\text{X}_n\text{T}_x$  (M represents a transition metal, X can be nitrogen and/or carbon, and  $\text{T}_x$  denotes surface functionalization) has attracted enormous consideration for the biosensing applications (Ghidiu et al., 2014; Khazaei et al., 2013; Naguib et al., 2011). Among them,  $\text{Ti}_3\text{C}_2$ -MXene is known for its metallic conductivity, super hydrophilicity, broad and strong absorption, polar surfaces, large surface area, which make them viable for electrochemical as well as fluorescent biosensors (Anasori et al., 2017; Kumar et al., 2018b;

Zhang et al., 2018). The ultrathin  $\text{Ti}_3\text{C}_2$ -MXene sheets terminated with oxygen and hydroxyl groups facilitate the material to communicate with a large number of biomolecules via hydrogen bonds, coordination bonds, van der Waals forces, and electrostatic interactions. Moreover,  $\text{Ti}_3\text{C}_2$ -MXene sheets exhibit wideband absorption in UV–vis region over its large surface area in conjunction with long-range electron and energy transferability, which enable the  $\text{Ti}_3\text{C}_2$ -MXene to become a prominent energy acceptor or quencher species (Shi et al., 2019; Zhang et al., 2018). Despite great potential, it has been observed that  $\text{Ti}_3\text{C}_2$ -MXene as a fluorescence quencher/energy acceptor is not explored much, and only a few attempts have been made in this direction (Peng et al., 2019; Shi et al., 2019; Zhang et al., 2018; Zhu et al., 2019). Unlike graphene,  $\text{Ti}_3\text{C}_2$ -MXene offers excellent aqueous solubility, superior surface terminated functionality, larger surface area, and better biocompatibility, preferable in the fabrication of efficient fluorescent biosensors (Song et al., 2020; Soomro et al., 2020). Besides, the self-reducing capability of  $\text{Ti}_3\text{C}_2$ -MXene exempt the requirement of additional reducing agent for decorating 0D nanomaterial on  $\text{Ti}_3\text{C}_2$ -MXene nanosheets.

Small cell lung cancer (SCLC) a distinct histological subgroup of lung cancer, is associated with poor prognosis, strong predilection for early metastasis, and exceptionally high proliferative rate (Rudin et al., 2021). SCLC is the most hostile form of lung cancer, accounting for around 15–20% of new cases. Besides, it is marked by acquired chemoresistance and high sensitivity to radiation and chemotherapy, and therefore difficult to cure (Jackman and Johnson, 2005). It can be life-threatening and metastasize to other body parts if not diagnosed at an initial stage. Therefore, there is an increased demand for SCLC's rapid and early detection, lowering the mortality rate. In this context, neuron specific enolase (NSE) is reported as an efficient biomarker for monitoring therapeutic treatment efficacy, disease progression, assessing tumor burden, and early diagnosis in view of its higher secretion rate (Amani et al., 2018; Han et al., 2012; Xiao et al., 2017). For healthy persons, the NSE concentration in serum can be up to 12–13  $\text{ng mL}^{-1}$  while SCLC patients have this concentration more than 35  $\text{ng mL}^{-1}$  (Harding et al., 1990; Kalkal et al., 2020; Shibayama et al., 2001). Quantitative detection of NSE in serum can be an exciting alternative for monitoring and clinical diagnosis of SCLC.

We report results of the studies relating to the fabrication and utilization of  $\text{Ag}@\text{Ti}_3\text{C}_2$ -MXene nanohybrid as a dual-energy acceptor for the development of a rapid, label-free, and highly sensitive fluorescent biosensor. The fabricated biosensor rely on the efficient trade-off between the donor (anti-NSE/amino-GQDs) and acceptor ( $\text{Ag}@\text{Ti}_3\text{C}_2$ -MXene) pair following the nanosurface energy transfer (NSET) mechanism. The  $\text{Ag}@\text{Ti}_3\text{C}_2$ -MXene nanohybrid based biosensor reveals improved biosensing characteristics in standard and spiked serum samples for NSE detection compared to bare  $\text{Ti}_3\text{C}_2$ -MXene, classic graphene and earlier reported AuNPs (Kalkal et al., 2020).

## 2. Materials and methods

### 2.1. Preparation of $\text{Ag}@\text{Ti}_3\text{C}_2$ -MXene nanohybrid

$\text{Ag}@\text{Ti}_3\text{C}_2$ -MXene nanohybrid has been obtained via the one-pot direct reduction of aqueous  $\text{AgNO}_3$  salt to AgNPs onto  $\text{Ti}_3\text{C}_2$ -MXene nanosheets. In this process, the 2D  $\text{Ti}_3\text{C}_2$ -MXene nanosheets acted both as a reducing agent and support matrix for AgNPs. Initially, 84.93 mg of  $\text{AgNO}_3$  is dispersed in 50 mL of deionized water through a vortex mixture to provide the 10 mM aqueous solution. On the other hand, 200 mg of powdered  $\text{Ti}_3\text{C}_2$ -MXene (supporting information, S3) is suspended in 20 mL of distilled water followed by ultrasonication for 30 min to provide the uniformly dispersed stock concentration (10  $\text{mg mL}^{-1}$ ). After that, 5 mL of dispersed  $\text{Ti}_3\text{C}_2$ -MXene with diluted concentrations (0.5, 1, 2, 5  $\text{mg mL}^{-1}$ ) is added in a dropwise manner to the above-prepared  $\text{AgNO}_3$  aqueous solution and continued stirring for 60 min. Fig. S1 shows the images of obtained  $\text{Ag}@\text{Ti}_3\text{C}_2$ -MXene nanohybrid

solution with different  $\text{Ti}_3\text{C}_2\text{-MXene}$  concentrations. The obtained solution of  $\text{Ag@Ti}_3\text{C}_2\text{-MXene}$  nanohybrid is centrifuged at 10,000 rpm and washed multiple times to remove the impurities. Finally, the resultant solution is vacuum dried to obtain the powdered  $\text{Ag@Ti}_3\text{C}_2\text{-MXene}$  nanohybrid.

## 2.2. Protein functionalization of amino graphene quantum dots (anti-NSE/amino-GQDs)

The hydrothermally synthesized amino-GQDs (supporting information, S4) are protein functionalized using the standard EDC-NHS coupling chemistry (Kalkal et al., 2020; Kumar et al., 2018a). To activate the carboxyl groups of monoclonal anti-NSE antibody, a solution containing 250  $\mu\text{L}$  of anti-NSE ( $50 \mu\text{g mL}^{-1}$ ), 125  $\mu\text{L}$  of NHS (0.05 M), and 125  $\mu\text{L}$  of EDC (0.2 M) is prepared and allowed to incubate for 30 min at room temperature. The activated anti-NSE antibody solution is mixed with an equal volume (500  $\mu\text{L}$ , 1:1 v/v) of amino-GQDs solution ( $20 \mu\text{g mL}^{-1}$ ) and incubated in a humid chamber for about 2 h. After that, the anti-NSE/amino-GQDs solution is ultra-centrifuged and washed with deionized water to remove the unbound antibodies. The protein functionalized GQDs are characterized by zeta potential, FTIR, and UV-vis techniques (supporting information (S6), Figs. S2c–e).

## 2.3. Design of fluorescent biosensor

The detection of target cancer biomarker is carried out in 50 mM phosphate-buffered saline (PBS) solution (pH 7.4) at room temperature by recording the fluorescence emission spectra. Here, 500  $\mu\text{L}$  of protein-functionalized amino-GQDs energy donor is mixed with 200  $\mu\text{L}$  of  $\text{Ag@Ti}_3\text{C}_2\text{-MXene}$  nanohybrid ( $50 \mu\text{g mL}^{-1}$ ) energy acceptor. After that, 50  $\mu\text{L}$  of distinct NSE concentrations ( $0.0001\text{--}1500 \text{ ng mL}^{-1}$ ) is added to the donor-acceptor mixture (anti-NSE/amino-GQDs/ $\text{Ag@Ti}_3\text{C}_2\text{-MXene}$ ) and allowed to incubate for an interval of 12 min. Consequently, the

alterations in fluorescence intensity are computed at the excitation wavelength of 360 nm with the increasing NSE antigen concentration in the resultant mixture. The selectivity studies of the fabricated biosensor have been performed by adding fixed concentration (50  $\mu\text{L}$ ,  $0.1 \text{ ng mL}^{-1}$ ) of various interfering biomarkers into anti-NSE/amino-GQDs/ $\text{Ag@Ti}_3\text{C}_2\text{-MXene}$  solution, followed by the measurement of corresponding emission spectra. The real sample analysis is performed in NSE spiked serum samples that are obtained from the hospital, Indian Institute of Technology Roorkee (IITR), after ethical approval by the Institutional Biosafety and Ethical Committee (BT/IHEC-IITR/2019/7525) (Pradhan et al., 2021b). 50  $\mu\text{L}$  of serum samples spiked with different NSE concentrations (10, 20, 50, 100, and 150  $\text{ng mL}^{-1}$ ) is added into the optimized donor-acceptor solution (anti-NSE/amino-GQDs/ $\text{Ag@Ti}_3\text{C}_2\text{-MXene}$ ) to record the corresponding emission spectra as described above.

## 3. Results and discussion

### 3.1. Mechanism of proposed fluorescent biosensor

The working of the proposed anti-NSE/amino-GQDs/ $\text{Ag@Ti}_3\text{C}_2\text{-MXene}$  biosensor is elaborated in a three-step process, and a schematic representation of the plausible mechanism is illustrated in Fig. 1. The driving force behind any fluorescent biosensor is based on the fluorescent state (ON/OFF) of the fluorophore, irrespective of its nature. In the first step, the fluorescence intensity of synthesized donor species (anti-NSE/amino-GQDs) is recorded at an excitation wavelength of 360 nm, which emit intense blue fluorescence around 450 nm (ON state). Secondly, the optimized amount of anti-NSE/amino-GQDs are physically adsorbed on the surface of  $\text{Ag@Ti}_3\text{C}_2\text{-MXene}$  nanohybrid through non-covalent interactions, which leads to an abrupt fluorescence quenching owing to dipole-surface interactions (OFF state). The  $\text{Ag@Ti}_3\text{C}_2\text{-MXene}$  nanohybrid acts as a dual-quencher in a single system for ultra-

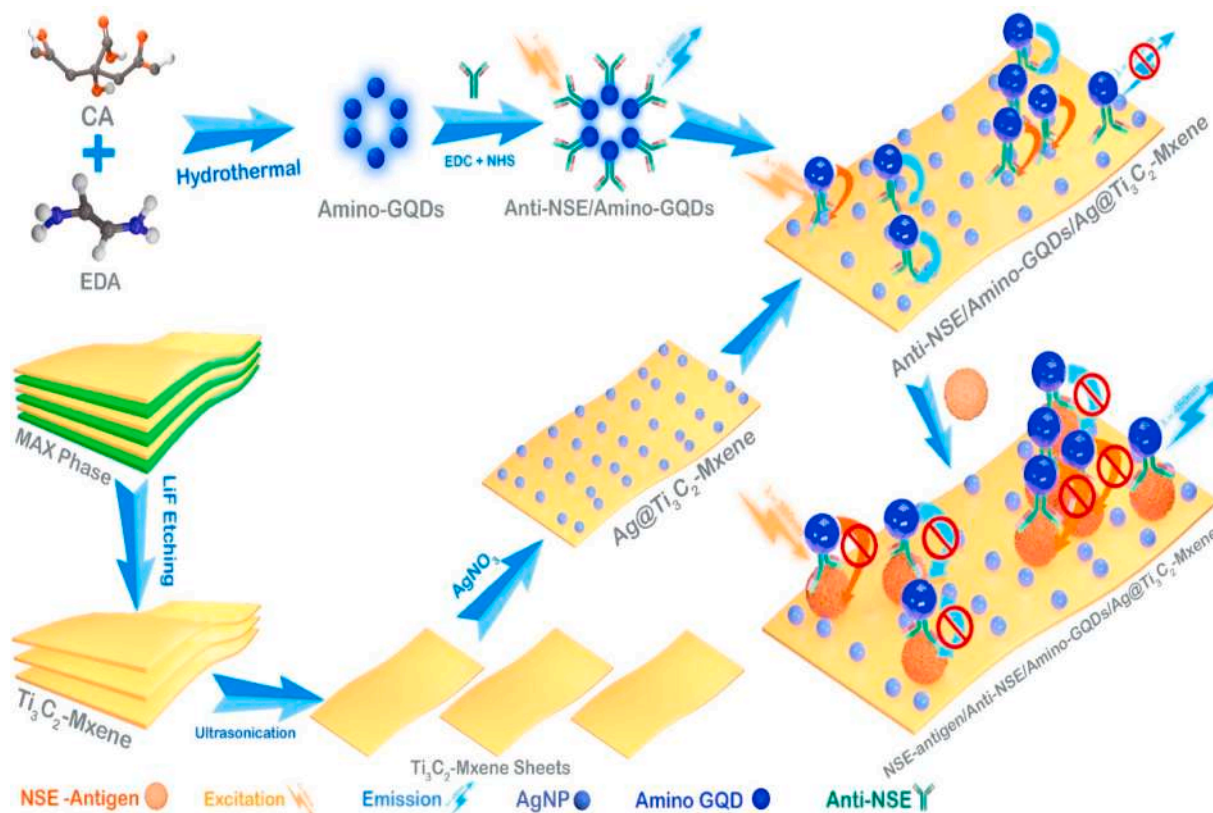


Fig. 1. Schematic illustration of anti-NSE/amino-GQDs/ $\text{Ag@Ti}_3\text{C}_2\text{-MXene}$  based biosensing platform for the fluorometric NSE detection.



high fluorescence quenching of donor species owing to their higher surface to volume ratio that enables effective energy transfer utilizing the concept of single-acceptor multiple-donor. In this context, the orange-colored arrows in Fig. 1 indicate the energy transfer to AgNPs from anti-NSE/amino-GQDs donor species. In contrast, energy transfer to  $\text{Ti}_3\text{C}_2\text{-MXene}$  nanosheets is shown with cyan-colored arrows. The 0D-2D complex of  $\text{Ag@Ti}_3\text{C}_2\text{-MXene}$  nanohybrid combines the benefit of both 0D AgNPs and 2D  $\text{Ti}_3\text{C}_2\text{-MXene}$  as individual energy acceptors. At last, the addition of the target antigen in the anti-NSE/amino-GQDs/ $\text{Ag@Ti}_3\text{C}_2\text{-MXene}$  biocomplex leads to specific immunocomplex (antigen-antibody) formation. Due to this, the fluorescence gets recovered (ON state) from the non-interacted anti-NSE/amino-GQDs donor as they detached from the  $\text{Ag@Ti}_3\text{C}_2\text{-MXene}$  nanohybrid surface due to the inferior non-covalent interactions. The recovered fluorescence from the donor species further relies on the added NSE concentration.

### 3.2. Characterizations of $\text{Ag@Ti}_3\text{C}_2\text{-MXene}$ nanohybrid

#### 3.2.1. Optical characterizations

The optical properties of synthesized  $\text{Ti}_3\text{C}_2\text{-MXene}$  and  $\text{Ag@Ti}_3\text{C}_2\text{-MXene}$  nanohybrid are identified from their corresponding colloidal solutions. The color of the synthesized  $\text{Ag@Ti}_3\text{C}_2\text{-MXene}$  nanohybrid complex appeared dark golden due to the reduction of  $\text{AgNO}_3$  to AgNPs by  $\text{Ti}_3\text{C}_2\text{-MXene}$  nanosheets (Fig. S1). Besides, the validation of

reduction has been studied through UV-vis spectroscopy (Fig. 2a), wherein initially a sharp absorption peak around 300 nm for  $\text{AgNO}_3$  salt and a broad peak around 270 nm for  $\text{Ti}_3\text{C}_2\text{-MXene}$  is observed (Kumar et al., 2018b). A continuous decrement in  $\text{AgNO}_3$  peak intensity and subsequently an increment in the intensity of AgNPs surface plasmon resonance (SPR) peak at 438 nm, with increasing concentrations of  $\text{Ti}_3\text{C}_2\text{-MXene}$  reflect the reduction and successful formation of  $\text{Ag@Ti}_3\text{C}_2\text{-MXene}$  nanohybrid (Pandey et al., 2018).

#### 3.2.2. Structural and morphological characterizations

The structural characterizations of synthesized AgNPs,  $\text{Ti}_3\text{C}_2\text{-MXene}$  and  $\text{Ag@Ti}_3\text{C}_2\text{-MXene}$  nanohybrid are investigated via XRD analysis (Fig. 2b). The AgNPs exhibits four sharp crystalline peaks associated to (111), (200), (220), and (311) planes at  $2\theta$  angle  $38.5^\circ$ ,  $44.7^\circ$ ,  $64.8^\circ$ , and  $77.7^\circ$ , respectively (JCPDS card no. 040783) (Zou et al., 2016). In  $\text{Ti}_3\text{C}_2\text{-MXene}$ , a weak and broad peak at  $2\theta = 6.8$  corresponding to (002) plane is observed, elucidating the formation of  $\text{Ti}_3\text{C}_2\text{-MXene}$  nanosheets (Kumar et al., 2018b). The spectrum of  $\text{Ag@Ti}_3\text{C}_2\text{-MXene}$  replicates the diffraction peaks of AgNPs and  $\text{Ti}_3\text{C}_2\text{-MXene}$ , indicating the nanohybrid formation. Interestingly, no peak shift has been observed in the spectrum of resultant nanohybrid that evince the decoration of AgNPs on the surface of  $\text{Ti}_3\text{C}_2\text{-MXene}$  nanosheets (Pandey et al., 2018).

The pivotal information such as surface chemical bonding, elemental composition, and the plausible direct reduction mechanism concerning

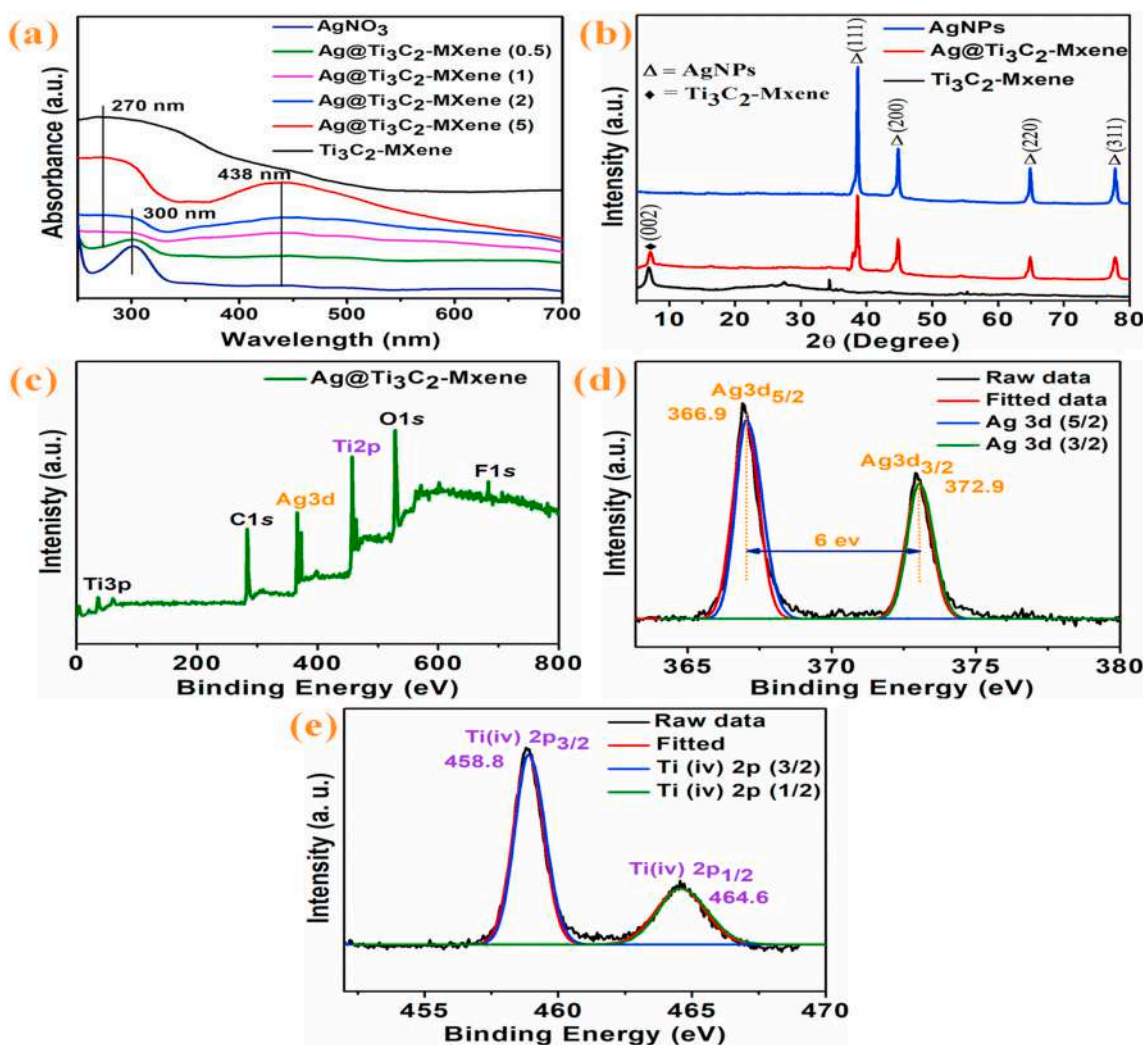


**Fig. 2.** (a) UV-vis absorption spectra of  $\text{Ti}_3\text{C}_2\text{-MXene}$ ,  $\text{Ag@Ti}_3\text{C}_2\text{-MXene}$  nanohybrid with different concentrations of  $\text{Ti}_3\text{C}_2\text{-MXene}$  (0.5, 1, 2, 5  $\text{mg mL}^{-1}$ ), and  $\text{AgNO}_3$  salt respectively; (b) Diffraction pattern of AgNPs,  $\text{Ag@Ti}_3\text{C}_2\text{-MXene}$  nanohybrid, bare  $\text{Ti}_3\text{C}_2\text{-MXene}$ ; (c) Full scan XPS profile of  $\text{Ag@Ti}_3\text{C}_2\text{-MXene}$  nanohybrid; (d) Deconvoluted Ag 3d spectra for  $\text{Ag@Ti}_3\text{C}_2\text{-MXene}$  nanohybrid; (e) Deconvoluted Ti 2p spectra for  $\text{Ag@Ti}_3\text{C}_2\text{-MXene}$  nanohybrid.

Ag@Ti<sub>3</sub>C<sub>2</sub>-MXene nanohybrid are investigated through XPS analysis. The full scan XPS spectra of the synthesized Ag@Ti<sub>3</sub>C<sub>2</sub>-MXene nanohybrid reveal the existence of C 1s, Ag 3d, O 1s, Ti 2p, Ti 3p, and F1s components (Fig. 2c). The detailed chemical bonding analysis of Ag and Ti have been elucidated by deconvoluting the Ag 3d and Ti 2p spectra. The deconvoluted Ag 3d spectra (Fig. 2d) comprises two prominent peaks related to Ag 3d<sub>3/2</sub> and Ag 3d<sub>5/2</sub> at the binding energy of 372.9, 366.9 eV, respectively, indicating the direct reduction of silver from Ag<sup>+</sup> to Ag(0) (Pandey et al., 2018). Additionally, the binding energy splitting is obtained 6 eV, demonstrating the presence of metallic AgNPs in the nanohybrid. Similarly, the deconvoluted Ti 2p spectra (Fig. 2e) comprises two main peaks at 458.8 and 464.6 eV related to Ti(iv) 2p<sub>3/2</sub>, and Ti(iv) 2p<sub>1/2</sub>, respectively (Zou et al., 2016). The self-reduction process provides the transformation of Ti (iii) and Ti (ii) to the terminated Ti (iv) species (Fig. 2e), validating the successful reduction of AgNO<sub>3</sub> to AgNPs by MXene nanosheets. This uniform deposition and self-reduction of AgNPs on Ti<sub>3</sub>C<sub>2</sub>-MXene nanosheets can be attributed to the activated low valence Ti species in the Ti<sub>3</sub>C<sub>2</sub>-MXene nanosheets (Pandey et al., 2018).

The detailed surface morphological analysis of synthesized Ti<sub>3</sub>C<sub>2</sub>-MXene and Ag@Ti<sub>3</sub>C<sub>2</sub>-MXene nanohybrid are investigated through TEM and FE-SEM characterizations. Stacked MXene flakes having flake sizes around 2–3 μm can be observed in the synthesized bare Ti<sub>3</sub>C<sub>2</sub>-MXene (Figs. S5–7). However, the Ag@Ti<sub>3</sub>C<sub>2</sub>-MXene nanohybrid indicates the

presence of non-aggregated and uniformly decorated AgNPs on ultrathin Ti<sub>3</sub>C<sub>2</sub>-MXene nanosheets (Fig. 3a–f). The energy dispersive X-ray spectroscopy (EDS) is also performed for the elemental spectrum, and mapping analysis. The EDS spectrum of Ti<sub>3</sub>C<sub>2</sub>-MXene (Fig. S3a) exhibits the occurrence of oxygen (O), carbon (C), and titanium (Ti) elements, whereas the spectrum of Ag@Ti<sub>3</sub>C<sub>2</sub>-MXene nanohybrid (Fig. S3b) reveals the existence of Ag along with O, C, and Ti. These elements are mapped with individual colors viz. yellow (Ag), turquoise (Ti), red (C), and green (O) for Ag@Ti<sub>3</sub>C<sub>2</sub>-MXene nanohybrid (Fig. 3h); and yellow (Ti), red (C), and green (O) for Ti<sub>3</sub>C<sub>2</sub>-MXene nanosheets (Fig. S4). Additionally, the line scan analysis is also carried out across the individual sheets, and their corresponding effects are depicted in Fig. S5 and Fig. 3i, which also evident the existence and distribution of these elements.

### 3.3. Steady-state and time-resolved spectroscopic studies between anti-NSE/amino-GQDs and Ag@Ti<sub>3</sub>C<sub>2</sub>-MXene nanohybrid

An effective energy transfer system requires an extensive selection of donor-acceptor pair that relies on the criteria of overlap between the emission spectra of donor species and absorption spectra of acceptor species (Neema et al., 2020). Herein, an optimal overlap has been obtained for the selected donor-acceptor pair, indicating the plausible energy transfer process (Fig. S8). Compared to previously reported

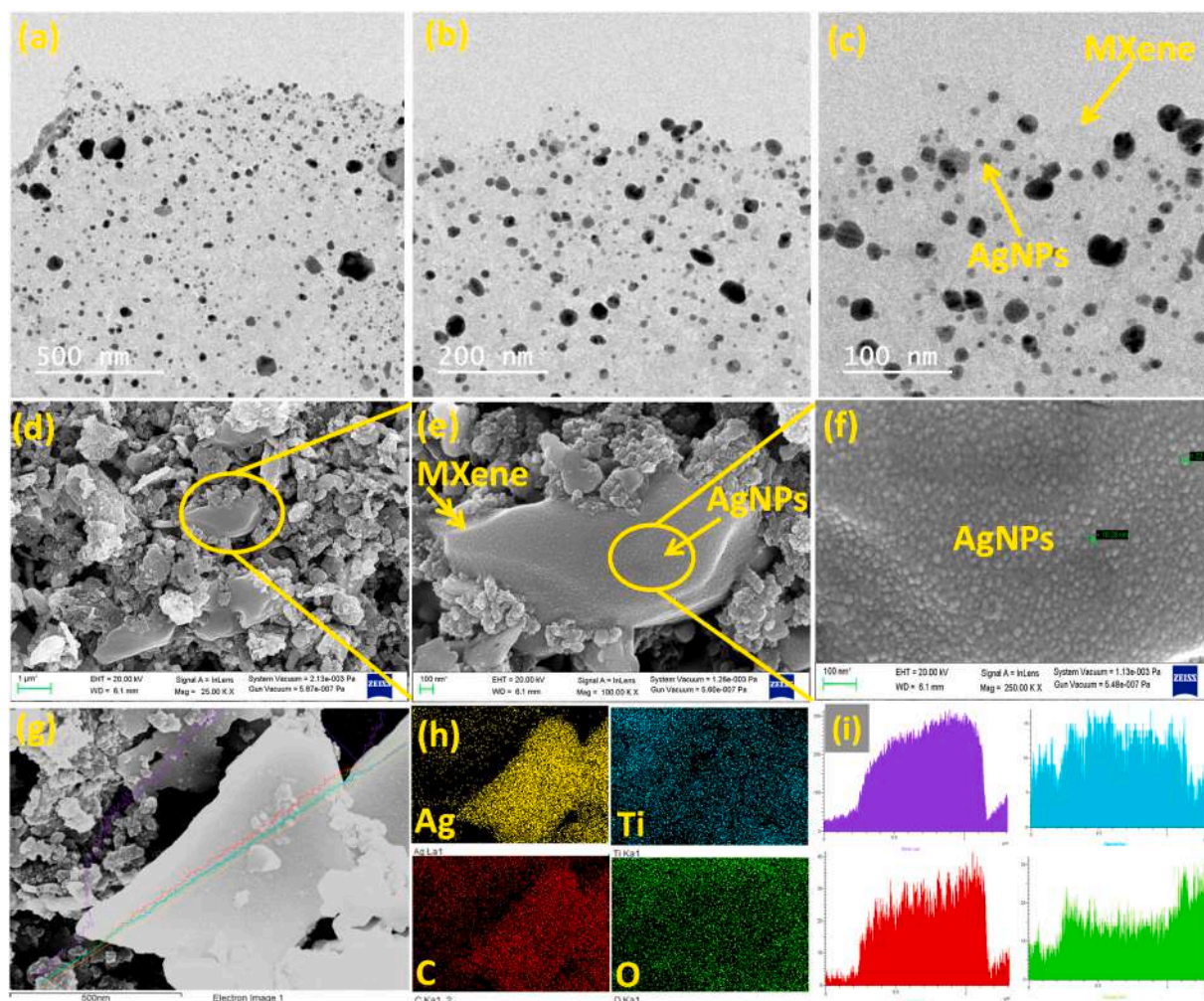


**Fig. 3.** (a–c) TEM images of Ag@Ti<sub>3</sub>C<sub>2</sub>-MXene nanohybrid at different scales, indicating the decoration of AgNPs on ultrathin Ti<sub>3</sub>C<sub>2</sub>-MXene nanosheets (d–g) FE-SEM images of Ag@Ti<sub>3</sub>C<sub>2</sub>-MXene nanohybrid at different magnifications; (h) Elemental mapping of Ag@Ti<sub>3</sub>C<sub>2</sub>-MXene nanohybrid revealing the presence of Ag (yellow), Ti (turquoise), C (red), and O (green) elements; (i) Line scan analysis of Ag@Ti<sub>3</sub>C<sub>2</sub>-MXene nanohybrid across the individual sheet. (For interpretation of the references to color in this figure legend, the reader is referred to the Web version of this article.)



AuNPs energy acceptor (Kalkal et al., 2020), the Ag@Ti<sub>3</sub>C<sub>2</sub>-MXene nanohybrid indicates better spectra overlap, signifying the improved energy transfer kinetics. The fluorescence quenching ability of Ag@Ti<sub>3</sub>C<sub>2</sub>-MXene nanohybrid has been compared with bare Ti<sub>3</sub>C<sub>2</sub>-MXene, AgNPs and earlier reported AuNPs. The protein-functionalized amino-GQDs are incubated with increasing concentrations of AgNPs, Ti<sub>3</sub>C<sub>2</sub>-MXene and Ag@Ti<sub>3</sub>C<sub>2</sub>-MXene nanohybrid followed by recording their corresponding emission spectra. It has been found that the fluorescence intensity of protein functionalized amino-GQDs decreases progressively after the addition of increasing concentrations of AgNPs (Fig. S9), Ti<sub>3</sub>C<sub>2</sub>-MXene (Fig. 4a), and Ag@Ti<sub>3</sub>C<sub>2</sub>-MXene (Fig. 4b) nanohybrid. This quenching can be attributed to the dipole-surface interactions between donor-acceptor pairs. The quenching efficiency (QE) with these materials was determined using Eq. (S1) and then compared. It has been observed that the Ag@Ti<sub>3</sub>C<sub>2</sub>-MXene exhibits higher quenching efficiency (~94%) compared to bare Ti<sub>3</sub>C<sub>2</sub>-MXene (~87%), AgNPs (~84) and AuNPs (~81%) (Kalkal et al., 2020). This increase in QE might be attributed to the synergistic effect of Ag@Ti<sub>3</sub>C<sub>2</sub>-MXene nanohybrid, which acts as a dual-quencher in a single system for the ultra-high fluorescence quenching of anti-NSE/amino-GQDs. The higher

surface to volume ratio of Ag@Ti<sub>3</sub>C<sub>2</sub>-MXene nanohybrid may enable efficient fluorescence quenching by introducing the concept of single-acceptor and multiple-donor (as depicted in Fig. 1). The integration of AgNPs to Ti<sub>3</sub>C<sub>2</sub>-MXene nanosheets offered a stable nanohybrid that may prevent the aggregation and stacking of bare AgNPs and Ti<sub>3</sub>C<sub>2</sub>-MXene nanosheets, respectively, resulting in enhanced QE.

Subsequently, the Stern-Volmer studies are examined to determine the quenching mechanism (Kumar et al., 2019a, 2020). In this context, Fig. 4d indicates the plots of  $F_0/F$  as a function of quencher concentration. The obtained linear plots signify the dynamic nature of quenching with both Ti<sub>3</sub>C<sub>2</sub>-MXene and Ag@Ti<sub>3</sub>C<sub>2</sub>-MXene (Swaminathan et al., 2017). Besides, the time-resolved fluorescence spectroscopy is carried out to study the nature of interactive energy transfer between donor-acceptor pair and measure the fluorescence lifetime of the donor in the presence and absence of quencher. Fig. 4e indicates the corresponding spectra of protein functionalized amino-GQDs with increasing Ag@Ti<sub>3</sub>C<sub>2</sub>-MXene concentrations. After the addition of increased Ag@Ti<sub>3</sub>C<sub>2</sub>-MXene concentration, the fluorescence lifetime of anti-NSE/amino-GQDs is observed to be progressively reduced, confirming the energy transfer mechanism from the anti-NSE/amino-GQDs

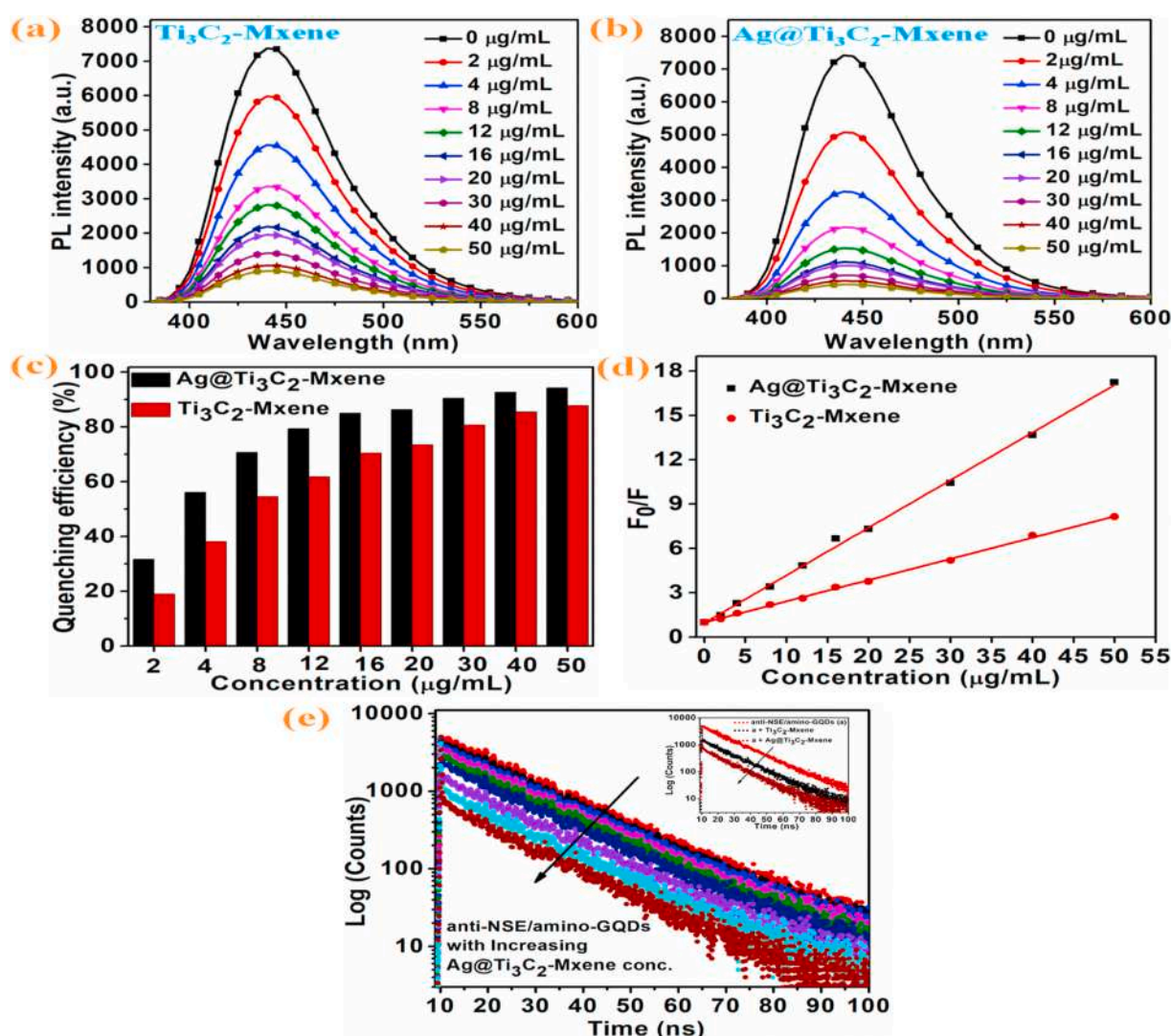


**Fig. 4.** Steady-state fluorescence quenching spectra of protein functionalized amino-GQDs with escalating concentrations (0–50 μg mL<sup>-1</sup> from top to bottom,  $\lambda_{\text{ex}}$  = 360 nm,  $\lambda_{\text{em}}$  ~ 450 nm); (a) bare Ti<sub>3</sub>C<sub>2</sub>-MXene (b) Ag@Ti<sub>3</sub>C<sub>2</sub>-MXene; (c) The comparison of fluorescence QE induced by Ti<sub>3</sub>C<sub>2</sub>-MXene and Ag@Ti<sub>3</sub>C<sub>2</sub>-MXene; (d) Stern-Volmer plot indicating the variation of  $F_0/F$  with different concentration of Ti<sub>3</sub>C<sub>2</sub>-MXene/Ag@Ti<sub>3</sub>C<sub>2</sub>-MXene from 0 to 50 μg mL<sup>-1</sup>; (e) Time-resolved fluorescence spectra of protein-functionalized amino-GQDs with increasing concentration of Ag@Ti<sub>3</sub>C<sub>2</sub>-MXene nanohybrid (inset shows the lifetime decay spectra of protein-functionalized amino-GQDs alone and with added Ti<sub>3</sub>C<sub>2</sub>-MXene and Ag@Ti<sub>3</sub>C<sub>2</sub>-MXene (200 μL, 0.05 mg mL<sup>-1</sup>).

to Ag@Ti<sub>3</sub>C<sub>2</sub>-MXene. In Fig. 4e, the downward inclined arrow states that the dynamics of emission decay become faster when the concentration of Ag@Ti<sub>3</sub>C<sub>2</sub>-MXene nanohybrid is increased. The protein functionalized amino-GQDs fluorescence lifetime follows bi-exponential decay dynamics with  $\tau_1 = 8.04$  ns (fast component), and  $\tau_2 = 16.64$  ns (slow component). Upon the addition of Ag@Ti<sub>3</sub>C<sub>2</sub>-MXene, the  $\tau_1$ ,  $\tau_2$  decrease from 8.04 to 2.4 ns and 16.64 to 15.26 ns, respectively. The inset of Fig. 4e indicates the lifetime decay spectra of protein-functionalized amino-GQDs alone and added Ti<sub>3</sub>C<sub>2</sub>-MXene and Ag@Ti<sub>3</sub>C<sub>2</sub>-MXene (200  $\mu$ L, 0.05 mg mL<sup>-1</sup>). The energy transfer performance of Ag@Ti<sub>3</sub>C<sub>2</sub>-MXene nanohybrid has been compared with bare Ti<sub>3</sub>C<sub>2</sub>-MXene and AuNPs (Kalkal et al., 2020), calculated using Eq. (1).

$$\varphi_E = 1 - \frac{\tau_{DA}}{\tau_D} \quad (1)$$

Where  $\tau_{DA}$  and  $\tau_D$  are the fluorescence lifetime of protein-functionalized amino-GQDs with and without quencher, respectively. It has been observed that the Ag@Ti<sub>3</sub>C<sub>2</sub>-MXene exhibits a higher energy transfer efficiency (~70%) compared to bare Ti<sub>3</sub>C<sub>2</sub>-MXene (~54) and AuNPs (43%) (Kalkal et al., 2020). This increased efficiency can be attributed to the prepared non-aggregated, unstaked, and stable Ag@Ti<sub>3</sub>C<sub>2</sub>-MXene

nanohybrid that might enable faster energy transfer kinetics from the donor species by working as an efficient dual-energy acceptor. The free conduction electrons present in AgNPs can facilitate in providing higher energy accepting capability through dipole vectors on their surface, high molecular extinction coefficient, and larger absorption spectra overlap near the Plasmon resonance frequency (Ghosh and Chattopadhyay, 2015). Furthermore, it is reported that AgNPs lack a defined dipole moment; thereby, energy transfer to AgNPs can occur in any orientation of donor species (Ghosh and Chattopadhyay, 2015; Shi et al., 2015). Apart from that, Ti<sub>3</sub>C<sub>2</sub>-MXene sheets exhibit wideband absorption in the UV-vis region over its large surface area in conjunction with long-range electron and energy transferability, providing improved energy transfer (Shi et al., 2019; Zhang et al., 2018).

#### 3.4. Analytical performance of the anti-NSE/amino-GQDs/Ag@Ti<sub>3</sub>C<sub>2</sub>-MXene based fluorescent biosensor

Under optimal conditions (supporting information (S7), Figs. S10–S11), the fluorescence spectroscopy has been carried out to explore the analytical performance of anti-NSE/amino-GQDs/Ag@Ti<sub>3</sub>C<sub>2</sub>-MXene (Fig. 5a) and anti-NSE/amino-GQDs/Ti<sub>3</sub>C<sub>2</sub>-MXene

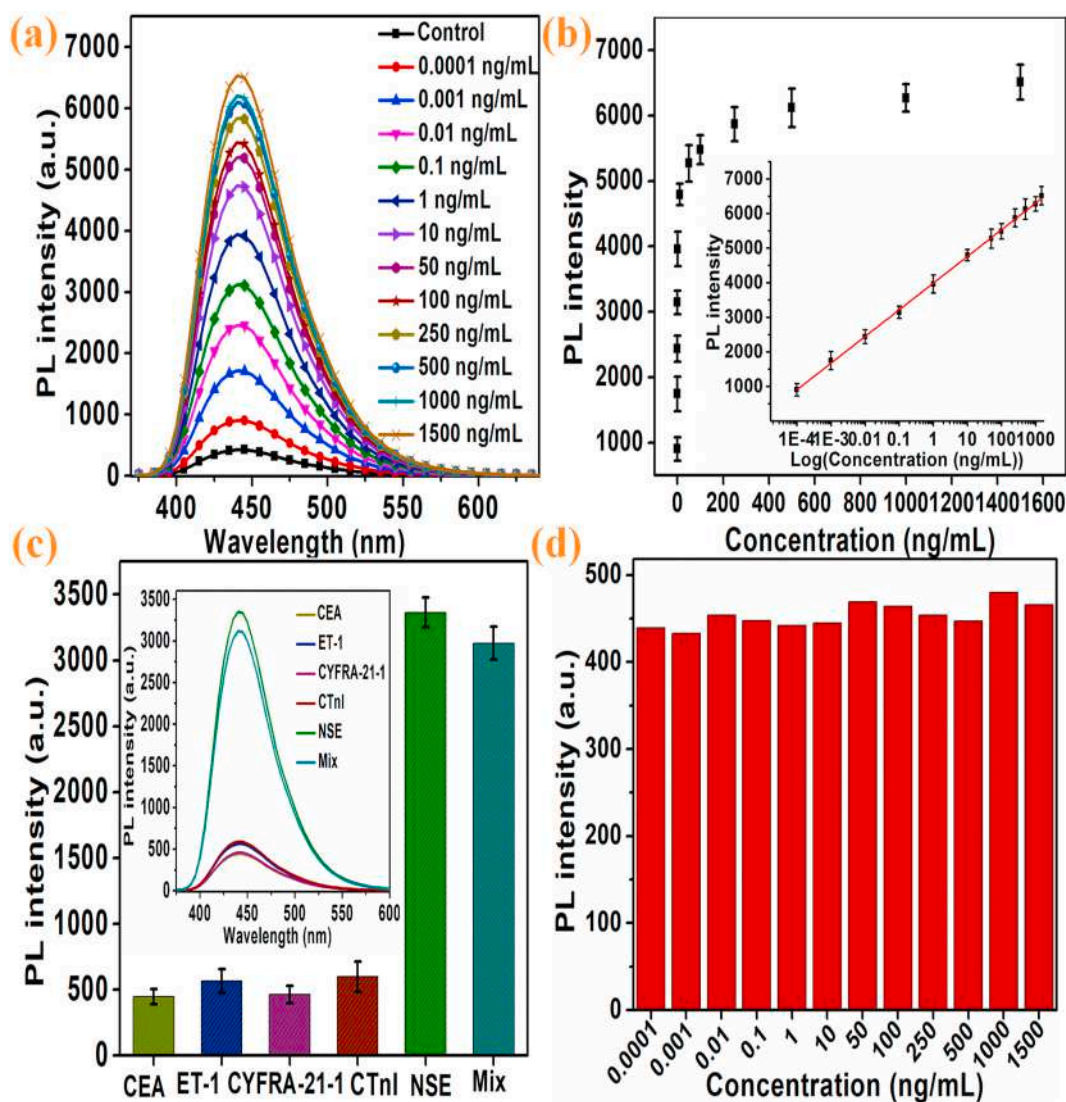


**Fig. 5.** (a) Analytical performance of the anti-NSE/amino-GQDs/Ag@Ti<sub>3</sub>C<sub>2</sub>-MXene based fluorescent biosensor toward NSE detection (b) Graph between recovered fluorescence and different NSE concentration, Inset indicates the corresponding calibration curve between recovered fluorescence and log NSE concentration in the range of 0.0001–1500 ng mL<sup>-1</sup> (c) Selectivity studies of proposed biosensor (d) Control experiment for the amino-GQDs/Ag@Ti<sub>3</sub>C<sub>2</sub>-MXene immunoelectrode.



(Fig. S12) based fluorescent immunosensing platforms toward different concentrations (0.0001–1500 ng mL<sup>-1</sup>) of NSE. It has been found that the fluorescence intensity of protein functionalized amino-GQDs restore with increasing NSE antigen concentration. The restoration in the fluorescence intensity is linearly correlated to the added concentration and can be ascribed to the formation of the antigen-antibody immunocomplex (Chen et al., 2018; Das et al., 2018). For each added concentration, the formed complex increases the distance among donor-acceptor species. Consequently, there will be no energy transfer from the protein-functionalized amino-GQDs to the Ag@Ti<sub>3</sub>C<sub>2</sub>-MXene/Ti<sub>3</sub>C<sub>2</sub>-MXene, and hence the fluorescence intensity starts to restore gradually. Fig. 5b and Fig. S12d indicate the calibration plot between recovered fluorescence intensities and log NSE concentration for anti-NSE/amino-GQDs/Ag@Ti<sub>3</sub>C<sub>2</sub>-MXene and anti-NSE/amino-GQDs/Ti<sub>3</sub>C<sub>2</sub>-MXene, respectively. In case of anti-NSE/amino-GQDs/Ag@Ti<sub>3</sub>C<sub>2</sub>-MXene, an established linear correlation is obtained in the dynamic range of 0.0001–1500 ng mL<sup>-1</sup>, described by the linear regression equation Eq. (2). Whereas, in case of anti-NSE/amino-GQDs/Ti<sub>3</sub>C<sub>2</sub>-MXene, a linear correlation is obtained in the range of 1–1000 ng mL<sup>-1</sup>, described by Eq. (S2).

$$I = 771.54 \log_{10} \text{NSE (ng mL}^{-1}) + 3987.04, \text{ the Regression coefficient } R^2 = 0.99 \quad (2)$$

Further, the limit of detection (LOD) is calculated according to the standard equation (Eq. S3). The LOD for anti-NSE/amino-GQDs/Ag@Ti<sub>3</sub>C<sub>2</sub>-MXene and anti-NSE/amino-GQDs/Ti<sub>3</sub>C<sub>2</sub>-MXene immunoprobe is calculated as 0.05 pg mL<sup>-1</sup> and 0.34 ng mL<sup>-1</sup>, respectively. Besides, we have compared the analytical performance of anti-NSE/amino-GQDs/Ag@Ti<sub>3</sub>C<sub>2</sub>-MXene fluorescent biosensor with classic 2D graphene (Fig. S13) and our previously reported AuNPs based sensing platforms. It is found that the anti-NSE/amino-GQDs/Ag@Ti<sub>3</sub>C<sub>2</sub>-MXene based biosensing platform exhibits better LOD, broader linear detection range, improved sensitivity, and a faster response time. Specifically, the sensitivity of Ag@Ti<sub>3</sub>C<sub>2</sub>-MXene based platform (~771 mL ng<sup>-1</sup>) is exceeding two times in contrast to graphene (~352 mL ng<sup>-1</sup>) as well as AuNPs (~333 mL ng<sup>-1</sup>) (Kalkal et al., 2020) based platforms. Furthermore, the biosensing characteristics of the present fluorescent biosensor are summarized in Table 1, along with reported aptasensors, sandwich assays, and immunosensors for NSE detection.

**Table 1**

Analytical comparison of anti-NSE/amino-GQDs/Ag@Ti<sub>3</sub>C<sub>2</sub>-MXene based biosensor with earlier reported biosensing platforms for NSE detection.

Sr. No.	Analytical Platform	Technique	Linear range (ng mL <sup>-1</sup> )	Limit of detection	Sensitivity	Time (min)	Ref.
1.	NH <sub>2</sub> -G/Thi/AuNPs POCT	Differential pulse Voltammetry (DPV)	1–500	10 pg mL <sup>-1</sup>	0.941 μA mL ng <sup>-1</sup>	18	Fan et al. (2017)
2.	MB-COOH/NH <sub>2</sub> -Apt-5	Chemiluminescence (CL)	1–100	0.1 ng mL <sup>-1</sup>	26.34 mL ng <sup>-1</sup>	–	Zheng et al. (2019)
3.	Fc-g-Au@Pd-P(BBY) and rGO/Thi/AuPt NAs	Electrochemical Impedance spectroscopy (EIS)	0.0001–50.0	0.03 pg mL <sup>-1</sup>	–	–	Chen et al. (2020)
4.	anti-NSE/DA/TiO <sub>2</sub> /FTO	Photocurrent	0.1–1000	0.05 ng mL <sup>-1</sup>	–	30	Li et al. (2017)
5.	CEA/anti-CEA/CNTs-AuNPs/GCE	Cyclic Voltammetry (CV)	0.10–200	0.04 ng mL <sup>-1</sup>	1.56 μA mL ng <sup>-1</sup>	20	Gao et al. (2011)
6.	FITC-anti-NSE/ALP-NSE/anti-FITC-MB	CL	0–300	0.2 ng mL <sup>-1</sup>	4774.8 mL ng <sup>-1</sup>	–	Fu et al. (2012)
7.	ITO/NiWO <sub>4</sub> /Ab	Photocurrent	75–723	0.12 ng mL <sup>-1</sup>	–	–	Soomro et al. (2019)
8.	HRP-P4/anti-P4/GCE	chronoamperometry	0.50–12.5	0.20 ng mL <sup>-1</sup>	3.0 ± 0.1 nA ng <sup>-1</sup> mL	15	Arévalo et al. (2010)
9.	anti-NSE/Au-Gra/NiHCFNPs/AuNCs/GCE	CV	0.001–100	0.3 pg mL <sup>-1</sup>	60.84 μA mL ng <sup>-1</sup>	30	Han et al. (2012)
10.	anti-NSE/amine-N-GQDs@AuNPs	Fluorescence Spectroscopy (FS)	0.0001–1000	0.09 pg mL <sup>-1</sup>	333.20 mL ng <sup>-1</sup>	16	Kalkal et al. (2020)
11.	anti-NSE/amino-GQDs/Ti <sub>3</sub> C <sub>2</sub> -MXene	FS	1–1000	0.34 ng mL <sup>-1</sup>	875.57 mL ng <sup>-1</sup>	–	This work
12.	anti-NSE/amino-GQDs/Ag@Ti <sub>3</sub> C <sub>2</sub> -MXene	FS	0.0001–1500	0.05 pg mL <sup>-1</sup>	771.54 mL ng <sup>-1</sup>	12	This work

### 3.5. Selectivity of the proposed fluorescent biosensor

The developed fluorescent biosensor has been found to exhibit good performance toward the detection of NSE biomarker. However, in human serum, various interfering biomarkers (other than NSE) such as cytokeratin-19 fragment (CYFRA-21-1), cardiac troponin-I (cTnI), endothelin-1 (ET-1), carcinoembryonic antigen (CEA) are also present. These interfering biomarkers may also contribute towards the fluorescence recovery of the fabricated biosensor. Therefore, it becomes crucial to examine the efficacy of developed biosensor in the presence of these potential serum biomarkers. In this context, Fig. 5c indicates the response of the biosensor in the presence of individual cancer biomarker (50 μL, 0.1 ng mL<sup>-1</sup>) and mixture of all biomarkers. A marginal recovery in fluorescence has been observed with interfering cancer biomarkers. The fluorescence recovery difference is estimated to be less than 5% when compared to the blank sample (anti-NSE/amino-GQDs/Ag@Ti<sub>3</sub>C<sub>2</sub>-MXene). Additionally, the selectivity coefficient (SC) is also determined for each biomarker utilizing Eq. (S5) and found to be ~1. In addition, the corresponding analytical signal is recorded to examine the selectivity of the immunosensor in a mixture of NSE and other mentioned biomarkers, which commensurate with the analytical signal linked to NSE alone, as shown in Fig. 5c. These findings explicitly suggest that fluorescence recovery is caused by specific NSE biomarker, demonstrating the excellent selectivity of the proposed fluorescent biosensor for NSE detection.

### 3.6. Control and reproducibility studies

Under similar conditions, the fluorescence response of the amino-GQDs/Ag@Ti<sub>3</sub>C<sub>2</sub>-MXene has been recorded in the same range (0.0001–1500 ng mL<sup>-1</sup>) as a controlled sample for NSE detection. The findings obtained (Fig. 5d) reveal that there is no substantial restoration of the fluorescence intensity against the added NSE concentration, suggesting that the restoration of fluorescence intensity is primarily due to the unique antibody-antigen interactions. Besides, fluorescent immunosensor reproducibility (Fig. S14) is determined by identifying NSE (50 μL, 1 ng mL<sup>-1</sup>) using five distinctive fluorescent probes fabricated under comparable conditions. The measured relative standard deviation of less than 10 percent (% RSD) signifies higher reproducibility and good accuracy.

### 3.7. Real sample analysis

For real sample analysis, the collected serum samples are spiked with 50  $\mu\text{L}$  of known NSE antigen concentrations (10, 20, 50, 100, and 150  $\text{ng mL}^{-1}$ ). Fig. S15a shows the results of the proposed immunosensor (anti-NSE/amino-GQDs/Ag@Ti<sub>3</sub>C<sub>2</sub>-MXene) toward five different NSE spiked serum samples. The incubation time of 12 min is provided for having the immunoreaction (antigen-antibody interactions) as in the previous experiment. For both the standard and spiked serum samples, a strong correlation suggesting a similar pattern of fluorescence intensity recovery has been obtained. The calibration plot between the fluorescence intensities and log of target biomarker concentration has been depicted in Fig. S15b. A linear relation has been realized, described by Eq. (S6). The % recovery in the spiked serum samples is determined using Eq. (3) and listed in Table S1.

$$\% \text{ recovery} = \frac{y_i - y_o}{y_s} \times 100 \quad (3)$$

Where  $y_s$  is the actual NSE spiked concentration and  $y_i$ ,  $y_o$  are the obtained concentrations in spiked and unspiked samples, respectively. The anti-NSE/amino-GQDs/Ag@Ti<sub>3</sub>C<sub>2</sub>-MXene based fluorescent immunosensor exhibit an average recovery of ~98%. The obtained results signify that the fabricated immunosensor can quantitatively detect the NSE biomarker in the clinical samples.

### 4. Conclusions

In the present work, a potential fluorescent biosensor comprised of biofunctionalized graphene quantum dots and Ag@Ti<sub>3</sub>C<sub>2</sub>-MXene nanohybrid is developed for the quantitative NSE detection. The functionality of this selective, rapid, label-free, and highly sensitive biosensor relies on the fluorescence quenching of donor species (anti-NSE/amino-GQDs) by the acceptor species (Ag@Ti<sub>3</sub>C<sub>2</sub>-MXene), followed by the restoration of quenched fluorescence upon the addition of NSE antigen. The Ag@Ti<sub>3</sub>C<sub>2</sub>-MXene nanohybrid as dual-energy acceptor exhibits higher quenching efficiency (~94%) compared to bare Ti<sub>3</sub>C<sub>2</sub>-MXene (~87%), AgNPs (~84%) and earlier reported AuNPs (~81%). Simultaneously, the energy transfer efficiency improved to 70% compared to Ti<sub>3</sub>C<sub>2</sub>-MXene (54%), and AuNPs (43%). Moreover, the developed Ag@Ti<sub>3</sub>C<sub>2</sub>-MXene nanohybrid-based biosensor exhibit improved biosensing parameters such as broader linear detection range (0.0001–1500  $\text{ng mL}^{-1}$ ), better LOD (0.05  $\text{pg mL}^{-1}$ ), higher sensitivity (~771  $\text{mL ng}^{-1}$ ), and faster response time (12 min). It is worth mentioning that the sensitivity of Ag@Ti<sub>3</sub>C<sub>2</sub>-MXene based biosensing platform is exceeding two times in contrast to classic graphene (~352  $\text{mL ng}^{-1}$ ) and our earlier reported AuNPs (~333  $\text{mL ng}^{-1}$ ) based platforms. On the other hand, enhanced linear detection range and LOD are observed in contrast to bare Ti<sub>3</sub>C<sub>2</sub>-MXene and graphene. The present biosensor also reveals remarkable performance in serum samples with ~98% average spiked NSE restoration. In nutshell, the developed immunosensor exhibits remarkable biosensing characteristics that make it a promising platform for quantitative NSE detection. Further efforts should be made towards integrating this potential platform with microfluidics and flexible electronics in creating the miniaturized point-of-care device.

### Declaration of competing interest

The authors declare that they have no known competing financial interests or personal relationships that could have appeared to influence the work reported in this paper.

### Acknowledgments

The present work is supported by the Department of Biotechnology (No. BT/PR25095/NER/95/1011/2017) Government of India. A. Kalkal

and S. Kadian are grateful to the Ministry of Education, India for the fellowship and Microfluidic Devices & Heterogeneous Systems Lab, Centre for Nano Science and Engineering (CeNSE), IISc, Bengaluru, India for the Internship. P. Gopinath would like to thank the Department of Science and Technology (DST), Government of India, Technology Innovation Hub (TIH) [A Section-8 Company: Divyasampark]. Saurabh Kumar acknowledges the DST for the DST-INSPIRE Faculty Award (DST/INSPIRE/04/2017/002750). Authors are thankful to the Centre of Nanotechnology, Department of Biosciences and Bioengineering IIT Roorkee and CeNSE, IISc, Bengaluru, India, for providing the required infrastructure and various characterization facilities.

### Appendix A. Supplementary data

Supplementary data to this article can be found online at <https://doi.org/10.1016/j.bios.2021.113620>.

### Author contributions

Ashish Kalkal, Saurabh kumar and P. Gopinath conceptualized the work. P. Gopinath, Saurabh Kumar, Prosenjit Sen, and Sumit Kumar provided valuable inputs and edited the manuscript. Ti<sub>3</sub>C<sub>2</sub>-MXene, Ag@Ti<sub>3</sub>C<sub>2</sub>-MXene nanohybrid synthesis, and optimization were carried out at CeNSE, IISc Bengaluru. Ti<sub>3</sub>C<sub>2</sub>-MXene and Ag@Ti<sub>3</sub>C<sub>2</sub>-MXene nanohybrid characterizations, biosensor fabrication, optimization, analysis and manuscript writing were performed by Ashish Kalkal. Sachin Kadian and Gaurav Manik provided their input in the XRD, UV, XPS, and PL characterizations. Sumit Kumar provided his input in performing the lifetime spectra. All authors contributed to draft the manuscript.

### References

- Amani, J., Maleki, M., Khoshroo, A., Sobhani-Nasab, A., Rahimi-Nasrabadi, M., 2018. An electrochemical immunosensor based on poly p-phenylenediamine and graphene nanocomposite for detection of neuron-specific enolase via electrochemically amplified detection. *Anal. Biochem.* 548, 53–59.
- Amjadi, M., Abolghasemi-Fakhri, Z., Hallaj, T., 2015. Carbon dots-silver nanoparticles fluorescence resonance energy transfer system as a novel turn-on fluorescent probe for selective determination of cysteine. *J. Photochem. Photobiol. Chem.* 309, 8–14.
- Anasori, B., Lukatskaya, M.R., Gogotsi, Y., 2017. 2D metal carbides and nitrides (MXenes) for energy storage. *Nature Reviews Materials* 2 (2), 16098.
- Arévalo, F.J., Messina, G.A., Molina, P.G., Zón, M.A., Raba, J., Fernández, H., 2010. Determination of progesterone (P4) from bovine serum samples using a microfluidic immunosensor system. *Talanta* 80 (5), 1986–1992.
- Atif, R., Inam, F., 2016. Reasons and remedies for the agglomeration of multilayered graphene and carbon nanotubes in polymers. *Beilstein J. Nanotechnol.* 7, 1174–1196.
- Bellunato, A., Arjmandi-Tash, H., Cesa, Y., Schneider, G.F., 2016. Chemistry at the Edge of Graphene 17 (6), 785–801.
- Bhatnagar, D., Kumar, V., Kumar, A., Kaur, I., 2016. Graphene quantum dots FRET based sensor for early detection of heart attack in human. *Biosens. Bioelectron.* 79, 495–499.
- Cha, J., Kyoung, W., Song, K., Park, S., Lim, T., Lee, J., Kang, H., 2016. Quantitative evaluation of the dispersion of graphene sheets with and without functional groups using molecular dynamics simulations. *Nanoscale research letters* 11 (1), 136–136.
- Chauhan, D., Pooja, Nirbhaya, V., Srivastava, C.M., Chandra, R., Kumar, S., 2020. Nanostructured transition metal chalcogenide embedded on reduced graphene oxide based highly efficient biosensor for cardiovascular disease detection. *Microchem. J.* 155, 104697.
- Chen, B., Su, Q., Kong, W., Wang, Y., Shi, P., Wang, F., 2018. Energy transfer-based biotransduction using optical nanomaterials. *J. Mater. Chem. B* 6 (19), 2924–2944.
- Chen, Y., Ge, X.-Y., Cen, S.-Y., Wang, A.-J., Luo, X., Feng, J.-J., 2020. Ultrasensitive dual-signal ratiometric electrochemical aptasensor for neuron-specific enolase based on Au nanoparticles@Pd nanoclusters-poly(bismarck brown Y) and dendritic AuPt nanoassemblies. *Sensor. Actuator. B Chem.* 311, 127931.
- Cui, S., Mao, S., Wen, Z., Chang, J., Zhang, Y., Chen, J., 2013. Controllable synthesis of silver nanoparticle-decorated reduced graphene oxide hybrids for ammonia detection. *Analyst* 138 (10), 2877–2882.
- Das, P., Sedighi, A., Krull, U.J., 2018. Cancer biomarker determination by resonance energy transfer using functional fluorescent nanoprobe. *Anal. Chim. Acta* 1041, 1–24.
- Fan, Y., Liu, J., Wang, Y., Luo, J., Xu, H., Xu, S., Cai, X., 2017. A wireless point-of-care testing system for the detection of neuron-specific enolase with microfluidic paper-based analytical devices. *Biosens. Bioelectron.* 95, 60–66.

- Fu, X., Meng, M., Zhang, Y., Yin, Y., Zhang, X., Xi, R., 2012. Chemiluminescence enzyme immunoassay using magnetic nanoparticles for detection of neuron specific enolase in human serum. *Anal. Chim. Acta* 722, 114–118.
- Gao, X., Zhang, Y., Wu, Q., Chen, H., Chen, Z., Lin, X., 2011. One step electrochemically deposited nanocomposite film of chitosan-carbon nanotubes-gold nanoparticles for carcinoembryonic antigen immunosensor application. *Talanta* 85 (4), 1980–1985.
- Ghidiu, M., Naguib, M., Shi, C., Mashtalir, O., Pan, L.M., Zhang, B., Yang, J., Gogotsi, Y., Billinge, S.J.L., Barsoum, M.W., 2014. Synthesis and characterization of two-dimensional Nb<sub>4</sub>C<sub>3</sub> (MXene). *Chem. Commun.* 50 (67), 9517–9520.
- Ghosh, D., Chattopadhyay, N., 2015. Gold and silver nanoparticles based superquenching of fluorescence: a review. *J. Lumin.* 160, 223–232.
- Han, J., Zhuo, Y., Chai, Y.-Q., Yuan, Y.-L., Yuan, R., 2012. Novel electrochemical catalysis as signal amplified strategy for label-free detection of neuron-specific enolase. *Biosens. Bioelectron.* 31 (1), 399–405.
- Harding, M., McAllister, J., Hulks, G., Vernon, D., Monie, R., Paul, J., Kaye, S.B., 1990. Neuron specific enolase (NSE) in small cell lung cancer: a tumour marker of prognostic significance? *Br. J. Canc.* 61 (4), 605–607.
- He, X., Zhang, S., Pan, H., Chen, J., Xu, J., 2019. Horizontally aggregation of monolayer reduced graphene oxide under deep UV irradiation in solution. *Nanoscale Research Letters* 14 (1), 117.
- Huang, K., Li, Z., Lin, J., Han, G., Huang, P., 2018. Two-dimensional transition metal catalysis and nitrides (MXenes) for biomedical applications. *Chem. Soc. Rev.* 47 (14), 5109–5124.
- Ikram, M., Raza, A., Imran, M., Ul-Hamid, A., Shahbaz, A., Ali, S., 2020. Hydrothermal synthesis of silver decorated reduced graphene oxide (rGO) nanoflakes with effective photocatalytic activity for wastewater treatment. *Nanoscale Research Letters* 15 (1), 95.
- Jackman, D.M., Johnson, B.E., 2005. Small-cell lung cancer. *Lancet* 366 (9494), 1385–1396.
- Kadian, S., Manik, G., Kalkal, A., Singh, M., Chauhan, R.P., 2019. Effect of sulfur doping on fluorescence and quantum yield of graphene quantum dots: an experimental and theoretical investigation. *Nanotechnology* 30 (43), 435704.
- Kalali, E.N., Guo, W., Wang, X., Xing, W., Song, L., Hu, Y., 2020. Effect of metal-based nanoparticles decorated graphene hybrids on flammability of epoxy nanocomposites. *Compos. Appl. Sci. Manuf.* 129, 105694.
- Kalkal, A., Allawadhi, P., Pradhan, R., Khurana, A., Bharani, K.K., Packirisamy, G., 2021a. Allium sativum derived carbon dots as a potential theranostic agent to combat the COVID-19 crisis. *Sensors International* 2, 100102.
- Kalkal, A., Kadian, S., Pradhan, R., Manik, G., Packirisamy, G., 2021b. Recent advances in graphene quantum dot-based optical and electrochemical (bio)analytical sensors. *Materials Advances* 2 (17), 5513–5541.
- Kalkal, A., Kumar, S., Kumar, P., Pradhan, R., Willander, M., Packirisamy, G., Kumar, S., Malhotra, B.D., 2021c. Recent advances in 3D printing technologies for wearable (bio)sensors. *Additive Manufacturing* 46, 102088.
- Kalkal, A., Pradhan, R., Kadian, S., Manik, G., Packirisamy, G., 2020. Biofunctionalized graphene quantum dots based fluorescence sensor toward efficient detection of small cell lung cancer. *ACS Applied Bio Materials* 3 (8), 4922–4932.
- Khazaei, M., Arai, M., Sasaki, T., Chung, C.-Y., Venkataramanan, N.S., Estili, M., Sakka, Y., Kawazoe, Y., 2013. Novel electronic and magnetic properties of two-dimensional transition metal carbides and nitrides. *Adv. Funct. Mater.* 23 (17), 2185–2192.
- Kumar, S., Ashish, Kumar, S., Augustine, S., Yadav, S., Yadav, B.K., Chauhan, R.P., Dewan, A.K., Malhotra, B.D., 2018a. Effect of Brownian motion on reduced agglomeration of nanostructured metal oxide towards development of efficient cancer biosensor. *Biosens. Bioelectron.* 102, 247–255.
- Kumar, S., Kalkal, A., 2021. 3 - electrochemical detection: cyclic voltammetry/differential pulse voltammetry/impedance spectroscopy. In: Khondakar, K.R., Kaushik, A.K. (Eds.), *Nanotechnology in Cancer Management*. Elsevier, pp. 43–71.
- Kumar, S., Kumar, J., Narayan Sharma, S., Srivastava, S., 2019a. rGO integrated MEHPV and P3HT polymer blends for bulk hetero junction solar cells: a comparative insight. *Optik* 178, 411–421.
- Kumar, Sumit, Sharma, Shailesh N., Kumar, Jitendra, 2019b. Comparative charge transport study of MEHPV-TiO<sub>2</sub> and P3HT-TiO<sub>2</sub> nanocomposites for hybrid bulk heterojunction solar cells. *J. Nanosci. Nanotechnol.* 6, 3408–3419. <https://doi.org/10.1166/jnn.2019.16130>.
- Kumar, S., Kumar, J., Sharma, S.N., 2020. Investigation of charge transfer properties in MEHPV and rGO-AA nanocomposites for Green organic photovoltaic application. *Optik* 208, 164540.
- Kumar, S., Lei, Y., Alshareef, N.H., Quevedo-Lopez, M.A., Salama, K.N., 2018b. Biofunctionalized two-dimensional Ti<sub>3</sub>C<sub>2</sub> MXenes for ultrasensitive detection of cancer biomarker. *Biosens. Bioelectron.* 121, 243–249.
- Kumar, S., Sharma, J.G., Maji, S., Malhotra, B.D., 2016. Nanostructured zirconia decorated reduced graphene oxide based efficient biosensing platform for non-invasive oral cancer detection. *Biosens. Bioelectron.* 78, 497–504.
- Li, H., Xiao, Q., Lv, J., Lei, Q., Huang, Y., 2017. Dopamine modified hyperbranched TiO<sub>2</sub> arrays based ultrasensitive photoelectrochemical immunosensor for detecting neuron specific enolase. *Anal. Biochem.* 531, 48–55.
- Liu, G., Zou, J., Tang, Q., Yang, X., Zhang, Y., Zhang, Q., Huang, W., Chen, P., Shao, J., Dong, X., 2017. Surface modified Ti<sub>3</sub>C<sub>2</sub> MXene nanosheets for tumor targeting photothermal/photodynamic/chemo synergistic therapy. *ACS Appl. Mater. Interfaces* 9 (46), 40077–40086.
- Mahdavi, M., Sharifpur, M., Ahmadi, M.H., Meyer, J.P., 2019. Aggregation study of Brownian nanoparticles in convective phenomena. *J. Therm. Anal. Calorim.* 135 (1), 111–121.
- Naguib, M., Kurtoglu, M., Presser, V., Lu, J., Niu, J., Heon, M., Hultman, L., Gogotsi, Y., Barsoum, M.W., 2011. Two-dimensional nanocrystals produced by exfoliation of Ti<sub>3</sub>AlC<sub>2</sub>. *Adv. Mater.* 23 (37), 4248–4253.
- Neema, P.M., Tomy, A.M., Cyriac, J., 2020. Chemical sensor platforms based on fluorescence resonance energy transfer (FRET) and 2D materials. *Trac. Trends Anal. Chem.* 124, 115797.
- Pandey, R.P., Rasool, K., Madhavan, V.E., Aissa, B., Gogotsi, Y., Mahmoud, K.A., 2018. Ultrahigh-flux and fouling-resistant membranes based on layered silver/MXene (Ti<sub>3</sub>C<sub>2</sub>Tx) nanosheets. *J. Mater. Chem.* 6 (8), 3522–3533.
- Peng, C., Yang, X., Li, Y., Yu, H., Wang, H., Peng, F., 2016. Hybrids of two-dimensional Ti<sub>3</sub>C<sub>2</sub> and TiO<sub>2</sub> exposing {001} facets toward enhanced photocatalytic activity. *ACS Appl. Mater. Interfaces* 8 (9), 6051–6060.
- Peng, X., Zhang, Y., Lu, D., Guo, Y., Guo, S., 2019. Ultrathin Ti<sub>3</sub>C<sub>2</sub> nanosheets based “off-on” fluorescent nanoprobe for rapid and sensitive detection of HPV infection. *Sensor. Actuator. B Chem.* 286, 222–229.
- Pradhan, R., Raisa, S.A., Jindal, S., Packirisamy, G., Manhas, S., 2021a. Four electrode-based impedimetric biosensors for evaluating cytotoxicity of tamoxifen on cervical cancer cells. *RSC Adv.* 11 (2), 798–806.
- Pradhan, R., Raisa, S.A., Kumar, P., Kalkal, A., Kumar, N., Packirisamy, G., Manhas, S., 2021b. Optimization, fabrication, and characterization of four electrode-based sensors for blood impedance measurement. *Biomed. Microdevices* 23 (1), 9.
- Rudin, C.M., Brambilla, E., Faivre-Finn, C., Sage, J., 2021. Small-cell lung cancer. *Nature Reviews Disease Primers* 7 (1), 3.
- Shao, K., Wang, L., Wen, Y., Wang, T., Teng, Y., Shen, Z., Pan, Z., 2019. Near-infrared carbon dots-based fluorescence turn on aptasensor for determination of carcinoembryonic antigen in pleural effusion. *Anal. Chim. Acta* 1068, 52–59.
- Shi, J., Tian, F., Lyu, J., Yang, M., 2015. Nanoparticle based fluorescence resonance energy transfer (FRET) for biosensing applications. *J. Mater. Chem. B* 3 (35), 6989–7005.
- Shi, Y.-e., Han, F., Xie, L., Zhang, C., Li, T., Wang, H., Lai, W.-F., Luo, S., Wei, W., Wang, Z., Huang, Y., 2019. A MXene of type Ti<sub>3</sub>C<sub>2</sub>Tx functionalized with copper nanoclusters for the fluorometric determination of glutathione. *Microchimica Acta* 187 (1), 38.
- Shibayama, T., Ueoka, H., Nishii, K., Kiura, K., Tabata, M., Miyatake, K., Kitajima, T., Harada, M., 2001. Complementary roles of pro-gastrin-releasing peptide (ProGRP) and neuron specific enolase (NSE) in diagnosis and prognosis of small-cell lung cancer (SCLC). *Lung Canc.* 32 (1), 61–69.
- Song, Q., Ye, F., Kong, L., Shen, Q., Han, L., Feng, L., Yu, G., Pan, Y., Li, H., 2020. Graphene and MXene nanomaterials. Toward High-Performance Electromagnetic Wave Absorption in Gigahertz Band Range 30 (31), 2000475.
- Soomro, R.A., Jawaid, S., Zhu, Q., Abbas, Z., Xu, B., 2020. A mini-review on MXenes as versatile substrate for advanced sensors. *Chin. Chem. Lett.* 31 (4), 922–930.
- Soomro, R.A., Kalwar, N.H., Avci, A., Pehlivan, E., Hallam, K.R., Willander, M., 2019. In-situ growth of NiWO<sub>4</sub> saw-blade-like nanostructures and their application in photoelectrochemical (PEC) immunosensor system designed for the detection of neuron-specific enolase. *Biosens. Bioelectron.* 141, 111331.
- Su, H., Zhang, C., Li, X., Wu, L., Chen, Y., 2018. Aggregation prevention: reduction of graphene oxide in mixed medium of alkylphenol polyoxyethylene (7) ether and 2-methoxyethanol. *RSC Adv.* 8 (68), 39140–39148.
- Sun, Y., Chen, D., Liang, Z., 2017. Two-dimensional MXenes for energy storage and conversion applications. *Materials Today Energy* 5, 22–36.
- Swaminathan, H., Ramar, V., Balasubramanian, K., 2017. Excited-state electron and energy transfer dynamics between 2D MoS<sub>2</sub> and GO/RGO for turn ON BSA/HSA sensing. *J. Phys. Chem. C* 121 (23), 12585–12592.
- Tian, F., Lyu, J., Shi, J., Yang, M., 2017. Graphene and graphene-like two-denominational materials based fluorescence resonance energy transfer (FRET) assays for biological applications. *Biosens. Bioelectron.* 89, 123–135.
- Tilaki, R.M., Irajizad, A., Mahdavi, S.M., 2006. Stability, size and optical properties of silver nanoparticles prepared by laser ablation in different carrier media. *Appl. Phys.* A 84 (1), 215–219.
- Torres-Mendieta, R., Ventura-Espinosa, D., Sabater, S., Lancis, J., Mínguez-Vega, G., Mata, J.A., 2016. In situ decoration of graphene sheets with gold nanoparticles synthesized by pulsed laser ablation in liquids. *Sci. Rep.* 6 (1), 30478.
- Vedala, H., Sorescu, D.C., Kotchey, G.P., Star, A., 2011. Chemical sensitivity of graphene edges decorated with metal nanoparticles. *Nano Lett.* 11 (6), 2342–2347.
- Xiao, K., Wang, K., Qin, W., Hou, Y., Lu, W., Xu, H., Wo, Y., Cui, D., 2017. Use of quantum dot beads-labeled monoclonal antibody to improve the sensitivity of a quantitative and simultaneous immunochromatographic assay for neuron specific enolase and carcinoembryonic antigen. *Talanta* 164, 463–469.
- Zhang, Q., Wang, F., Zhang, H., Zhang, Y., Liu, M., Liu, Y., 2018. Universal Ti<sub>3</sub>C<sub>2</sub> MXenes based self-standard ratiometric fluorescence resonance energy transfer platform for highly sensitive detection of exosomes. *Anal. Chem.* 90 (21), 12737–12744.
- Zheng, Y., Zhao, Y., Di, Y., He, L., Liao, S., Li, D., Liu, X., 2019. In vitro selection of DNA aptamers for the development of chemiluminescence aptasensor for neuron-specific enolase (NSE) detection. *RSC Adv.* 9 (27), 15513–15520.
- Zhou, H., Wu, F., Fang, L., Hu, J., Luo, H., Guan, T., Hu, B., Zhou, M., 2020. Layered NiFe-LDH/MXene nanocomposite electrode for high-performance supercapacitor. *Int. J. Hydrogen Energy* 45 (23), 13080–13089.
- Zhu, X., Pang, X., Zhang, Y., Yao, S., 2019. Titanium carbide MXenes combined with red-emitting carbon dots as a unique turn-on fluorescent nanosensor for label-free determination of glucose. *J. Mater. Chem. B* 7 (48), 7729–7735.
- Zou, G., Zhang, Z., Guo, J., Liu, B., Zhang, Q., Fernandez, C., Peng, Q., 2016. Synthesis of MXene/Ag composites for extraordinary long cycle lifetime lithium storage at high rates. *ACS Appl. Mater. Interfaces* 8 (34), 22280–22286.